https://doi.org/10.5194/egusphere-2025-3215
Preprint. Discussion started: 4 September 2025

Atmospheric CO_2 dynamics in a coastal megacity: spatiotemporal patterns, sea-land breeze impacts, and anthropogenic-biogenic emission partitioning

Jinwen Zhang[1], Yongjian Liang[2], Chenglei Pei[2], Bo Huang[3], Yingyan Huang[2], Xiufeng Lian[1,3], Shaojie Song[4], Chunlei Cheng[1], Cheng Wu[1], Zhen Zhou[1], Junjie Li[5], Mei Li[1*]

[1]College of Environment and Climate, Institute of Mass Spectrometry and Atmospheric Environment, Guangdong Provincial Engineering Research Center for Online Source Apportionment System of Air Pollution, Guangdong-Hongkong-Macau Joint Laboratory of Collaborative Innovation for Environmental Quality, Jinan University, Guangzhou 511443, China
[2]Guangzhou Ecological and Environmental Monitoring Center Station, Guangdong, Guangzhou 510006, China
[3]Guangzhou Hexin Instrument Co., Ltd., Guangdong, Guangzhou 510530, China
[4]College of Environmental Science and Engineering, Nankai University, Tianjin 300350, China
[5]School of Environment, Beijing Jiaotong University, Beijing 100044, China

Correspondence to: Mei Li (limei@jnu.edu.cn)

Abstract. Accurate quantification of urban carbon dioxide (CO_2) emissions is essential for evaluating the efficacy of urban climate mitigation policies. However, the complex interplay of anthropogenic emissions, biogenic fluxes, and meteorological processes in coastal megacities poses significant challenges to characterizing urban CO_2 dynamics. To address this, we present an observation-based framework that integrates high-precision CO_2 monitoring, meteorological analyses, and $\Delta CO/\Delta CO_2$ ratios (Rco) to resolve spatiotemporal CO_2 variations, quantify sea-land breeze (SLB) effects, and partition anthropogenic and biogenic contributions. Applied in Guangzhou, a coastal megacity, our approach captures a pronounced urban–rural gradient. The coastal site shows the largest seasonal amplitude (25.63 ppm), resulting from wintertime transport of urban emissions and summertime inflow of marine air. Diurnally, suburban CO_2 variations are dominated by biogenic activity (summer amplitude: 39.90 ppm), while urban signals reflect anthropogenic influence. SLB generally reduces coastal CO_2 by 5.87 ppm but leads to a summer accumulation (+2.08 ppm) under stable, low-wind conditions with shallow boundary layers. Regression-derived Rco values (urban: 7.45 ± 1.38 ppb ppm^{-1}) reflect improved combustion efficiency linked to clean-air policies. Importantly, our combined observational, modeling, and Rco framework reveals that biogenic fluxes offset 60.17% of anthropogenic CO_2 emissions during summer afternoons. The framework is validated against emission inventories, Normalized Difference Vegetation Index data, and independent studies, demonstrating its robustness. This study enhances process-oriented understanding of coastal carbon cycling and underscores the integration of meteorological and biospheric dynamics in urban CO_2 assessments.

1 Introduction

Atmospheric carbon dioxide (CO_2), the predominant anthropogenic driver of climate change, is accumulating at unprecedented

https://doi.org/10.5194/egusphere-2025-3215
Preprint. Discussion started: 4 September 2025

rates in human history (WMO, 2024). Future CO_2 increments will exert stronger warming effects than equivalent past increases due to climate system feedbacks (He et al., 2023), making emission control imperative. Despite covering only 3 % of global land, urban areas generate over 70 % of carbon emissions (Crippa et al., 2021), positioning them as critical climate mitigation targets. As fundamental administrative units capable of implementing carbon-reduction strategies, cities require high-precision CO_2 monitoring to validate policy efficacy against emission goals.

High-precision monitoring of atmospheric CO_2 emissions in coastal megacities is critically urgent due to their dual role as economic powerhouses and climate vulnerability hotspots. These regions exhibit intensive industrialization, dense populations, and high fossil fuel consumption, driving disproportionate emissions of greenhouse gases and air pollutants (Shan et al., 2020; Li et al., 2022; Cai et al., 2023) that exacerbate climate change and health risks (Patz et al., 2014). All ten cities most impacted by climate-amplified natural disasters are coastal, highlighting their acute vulnerability (Kumar, 2021). Characterizing urban CO_2 dynamics remains challenging due to complex terrain, unique land-sea weather systems (particularly diurnal sea-land breezes), heterogeneous vegetation distribution, and seasonal biogenic fluxes (Leroyer et al., 2014; Lei et al., 2024; Raciti et al., 2014; Järvi et al., 2012). While single-site studies and aircraft measurements have quantified temporal CO_2 variations and anthropogenic components (Wei et al., 2020; Pitt et al., 2022; Newman et al., 2013; Niu et al., 2016; Ishidoya et al., 2020), they fail to resolve coastal spatiotemporal heterogeneity or disentangle meteorological, anthropogenic, and biogenic drivers across diverse landscapes. Critical knowledge gaps persist despite multi-site analyses in cities like Boston, Portland, Helsinki, and San Francisco linking spatial variability to meteorology and local sources (Briber et al., 2013; Rice and Bostrom, 2011; Kurppa et al., 2015; Shusterman et al., 2018), and methods for marine background screening (Verhulst et al., 2017). Persistent knowledge gaps critically constrain coastal carbon research: (1) systematic analyses of coastal-specific weather systems (notably sea-land breezes) on CO_2 dynamics remain absent; (2) emission inventories persistently neglect quantitative assessment of biogenic fluxes; and crucially, (3) biogenic contributions to urban carbon budgets continue to lack robust constraints. This triad of limitations fundamentally impedes the mechanistic understanding of coastal megacity carbon cycles and undermines evidence-based mitigation strategies.

Sea-land breeze (SLB) circulation, a ubiquitous mesoscale phenomenon in coastal zones driven by land-sea thermal contrast (Chen et al., 2016; Shen et al., 2021), is intensifying under climate change: frequency has increased across 70 % of China's coastline over five decades due to widening land-ocean temperature differentials (Huang et al., 2025). Although SLB significantly influences coastal air quality (Nie et al., 2020; Zhao et al., 2022; Wang et al., 2023; Zheng et al., 2024), its impacts on urban CO_2 dynamics are unexplored. Short-term modeling suggests that daytime coastal CO_2 measurements may be contaminated by SLB-advected respired CO_2 from the vegetation during the previous night, potentially biasing emission

https://doi.org/10.5194/egusphere-2025-3215
Preprint. Discussion started: 4 September 2025

inversions (Ahmadov et al., 2007). Preliminary trajectory analyses hint at SLB's importance in diurnal greenhouse gas variability (Verhulst et al., 2017), while SLB-mediated cooling/humidification may enhance carbon uptake in subtropical mangroves (Zhu et al., 2021). Thus, investigating SLB-CO_2 interactions is imperative for advancing coastal carbon cycle science.

Urban vegetation constitutes a significant carbon reservoir, yet its contribution to carbon sequestration is frequently underestimated in urban carbon budgets (Davies et al., 2011; Raciti et al., 2014; Gough and Elliott, 2012).Urbanization-induced microclimates—notably extended the urban growing seasons (Melaas et al., 2016a; Melaas et al., 2016b)—stimulate aboveground biomass accumulation, yielding growth rates equivalent to some forests, while also enhancing vegetation net ecosystem exchange (Zhao et al., 2012; Briber et al., 2013; Briber et al., 2015). Yet, observational quantification of urban-scale biogenic fluxes remains scarce. While radiocarbon (^{14}C) measurements provide robust fossil/biogenic partitioning (Turnbull et al., 2015; Niu et al., 2016; Berhanu et al., 2017; Wang et al., 2022), their cost and discontinuous sampling limit applicability. Eddy covariance measurements quantify net CO_2 fluxes within tower footprints (typically 1–2 km radius), yet the derived flux partitioning reflects only local-scale dynamics and cannot represent city-wide carbon exchange processes (Velasco et al., 2013; Menzer and Mcfadden, 2017; Sugawara et al., 2021; Wu et al., 2022b). Inversion models incorporating co-emitted tracers (e.g., CO and NO_2) and isotopes face challenges from prior emission uncertainties and computational demands (Feng et al., 2024; Newman et al., 2016; Gómez-Ortiz et al., 2025).

To elucidate atmospheric CO_2 dynamics in coastal megacities and bridge critical knowledge gaps in urban carbon cycling, this study investigates Guangzhou—a representative Chinese coastal megacity—as a living laboratory. Guangzhou—a subtropical coastal megacity ranking fourth among Chinese cities in annual GDP (population: 18.83 million)—features 43.77 % green coverage, a pronounced maritime climate, and frequent SLB events (Qiu and Fan, 2013a; Mai et al., 2024b). Its high-precision greenhouse gas monitoring network (covering urban, suburban, and coastal zones) with > 1.5 years of observations provides an ideal platform for this study.

In this study, we analyze spatiotemporal heterogeneity in urban CO_2 concentrations and dissect the differential roles of anthropogenic emissions, biogenic fluxes, and meteorological processes across urban, suburban, and coastal landscapes. This approach advances understanding of urban-scale drivers governing CO_2 distribution patterns. Further, we employ an observation-based diagnostic method using meteorological tower data to quantify SLB impacts on CO_2 dynamics and their underlying mechanisms, addressing a fundamental gap in coastal carbon cycle science. Complementing this, we develop a parsimonious framework integrating observational data, atmospheric transport modeling, and CO/CO_2 emission ratios to

https://doi.org/10.5194/egusphere-2025-3215
Preprint. Discussion started: 4 September 2025

partition anthropogenic (CO_2ff) and biogenic (CO_2bio) fluxes. This cost-effective strategy enables robust assessment of biogenic contributions to urban carbon budgets, validated against bottom-up emission inventories, the NDVI and independent studies. The resulting methodological framework provides a transferable blueprint for global coastal megacity carbon research and offers scientific foundations for evidence-based urban climate mitigation policy design and efficacy evaluation.

2 Data and methodology

2.1 Observational sites

The high-precision greenhouse gas monitoring network in Guangzhou is illustrated in Fig. 1. Three stations—Nansha (NS), Panyu (PY), and Conghua (CH) are symmetrically distributed along the city's predominant south-north wind axis, representing coastal, urban, and suburban atmospheric conditions, respectively. Site selection criteria are detailed in the Supplement. All stations employ tower-based sampling at similar heights: NS and PY at 48 m, and CH at 40 m. Monitoring spanned from January 1, 2023, to September 30, 2024. From PY, the straight-line distances to NS and CH are 54 km and 89 km, respectively.

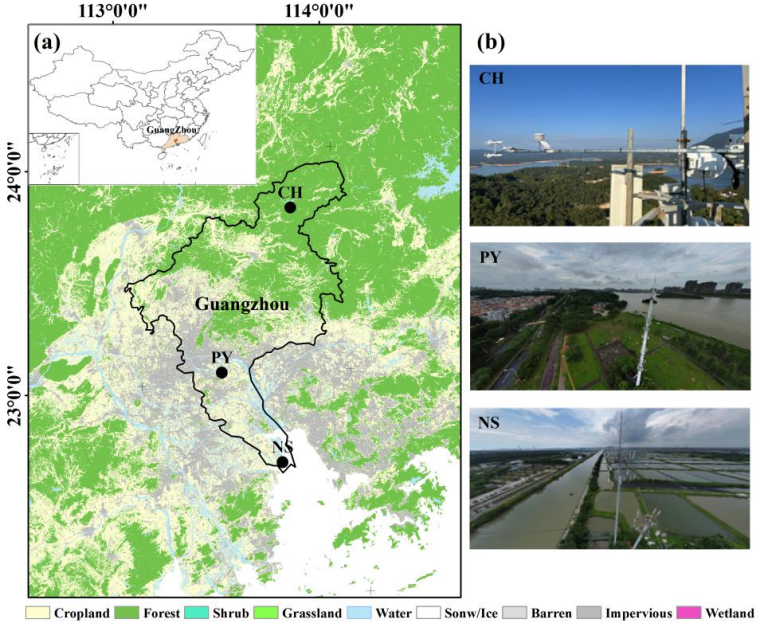

Figure 1. (a) Geographic locations of the NS, PY, and CH stations, with regional land use classification based on the 30 m resolution 2023 CLCD data (Yang and Huang, 2025). (b) Photograph of each station.

The NS station (113.63° E, 22.61° N) is located < 5 km from the coastline. This coastal site is surrounded by aquaculture ponds and sparse wetlands. Infrastructure nearby includes the under-construction southern extension of Guangzhou Metro Line 18 (NW direction) and the S78 highway (2 km west). The PY station (113.38° E, 23.03° N) is situated in the densely populated urban core, the tower is adjacent to Guangzhou University Town (north) and the Pearl River (south). A city road (100 m north)

https://doi.org/10.5194/egusphere-2025-3215
Preprint. Discussion started: 4 September 2025

and the S73 expressway (700 m west) contribute to local emissions. The CH station (113.78° E, 23.74° N) is positioned in the northern suburbs. The site is bordered by subtropical evergreen broadleaf forests (north), a tourist resort (south), and a tea processing plant. The G45 highway lies 3 km northwest. According to the 2023 EDGAR global emission inventory (Crippa et al., 2024), grid-level CO_2 emissions for NS, PY, and CH are 3456, 15244, and 203 ton km^{-2} yr^{-1}, respectively (Fig. S1 in the Supplement).

2.2 Monitoring system

All three stations are equipped with similar monitoring systems, consisting of sampling modules, calibration modules, gas analyzers, and data acquisition systems. Notably, the NS and PY stations utilize Picarro G2401 greenhouse gas analyzers to measure CO_2/CH_4/CO/H_2O, with a CO_2 measurement precision of < 20 ppb (5 min, 1 σ). The CH station employs an ABB GLA331-GGA greenhouse gas analyzer to measure CO_2/CH_4/H_2O, with a CO_2 measurement precision of < 25 ppb (5 min, 1 σ). N_2O and CO are measured using a GLA351-N2OCM analyzer. Detailed monitoring system and principles of the instruments are provided in the Supplement. Prior to field deployment, comparative tests were conducted in the laboratory to ensure the analytical performance consistency of the instruments. Additionally, meteorological sensors (measuring wind speed, direction, humidity, temperature, and pressure) are installed at the same height as the sampling inlets at NS and PY stations, while the CH station lacks such sensors. Detailed descriptions of wind field characteristics at NS and PY stations are included in the Supplement and illustrated in Fig. S2.

2.3 Calibration methods

The calibration module comprises two components: working standard curve establishment and target gas verification. High- and low-concentration standard gases are used to establish calibration curves, while a mid-concentration standard gas is used for target verification. The target and calibration gases are stored in inert-coated aluminum cylinders, uniformly supplied by the China National Environmental Monitoring Center. All stations follow the same calibration protocol: (1) weekly calibration curve establishment: high- and low-concentration gases are injected for 30 minutes each, with the final 5 minutes of instrument response used for calibration; (2) target gas verification every 12 hours: mid-concentration gas is injected for 30 minutes, with the final 5 minutes of response used for verification; (3) re-calibration is triggered if the residual value (H) from target verification exceeds ± 0.2 ppm.

Calibration curves are derived from the instrument's response to calibration gas, yielding a linear calibration equation:

$$Y = A \times X - B, \quad (1)$$

where A, B are calibration coefficients. Calibrated CO_2 ($CO_{2,k}$) is calculated by:

https://doi.org/10.5194/egusphere-2025-3215
Preprint. Discussion started: 4 September 2025

$$CO_{2,k} = A \times CO_{2,m} - B \,, \quad (2)$$

where $CO_{2,m}$ is the measured response. Daily 12-hour target gas verification is conducted to assess analyzer accuracy and stability by calculating the residual H:

$$H = \left(A \times CO_{2,c} - B\right) - CO_{2,n} \quad . \quad (3)$$

where $CO_{2,n}$ is the standard CO_2 concentration of the target gas, where $CO_{2,c}$ is the analyzer response to the target gas.

To ensure high-precision and stable monitoring results, periods with $|H| \leqslant 0.1$ ppm are prioritized. Measurement uncertainties for the analyzers at NS, PY, and CH stations, calculated as the standard deviation (SD) of H (Yang et al., 2021), are 0.04, 0.02, and 0.04 ppm, respectively. In addition to daily calibration, maintenance personnel conduct weekly inspections of instruments and station facilities, including checks on power supply stability, data logger functionality, and industrial control computer status. Consumables (e.g., filters) are replaced as needed, and emergency repairs or instrument overhauls are performed when necessary. Any instrument downtime caused by internal or external factors is documented in maintenance logs, and affected data is flagged. Throughout the monitoring period, all three stations maintained data validity rates exceeding 90 %.

2.4 Sea-land breeze identification

The straight-line distances from the NS, PY, and CH stations to the coastline are 4, 58, and 130 km, respectively. The NS station, closest to the coast, was selected to study Guangzhou's sea-land breeze (SLB) circulation. Prior to SLB identification, local and background winds must be differentiated, as tower-measured winds (Fig. S2 in the Supplement) represent superimposed local and background wind fields, where strong background winds can obscure SLB signals (Qiu and Fan, 2013b). The following equations distinguish background winds from local winds (Sun et al., 2022):

$$U_b = \overline{\sum_{i=0}^{23} U_i} \,, \quad (4)$$

$$V_b = \overline{\sum_{i=0}^{23} V_i} \,, \quad (5)$$

$$U_l = U_O - U_b \,, \quad (6)$$

$$V_l = V_O - V_b \,. \quad (7)$$

where U_O and V_O are the observed wind fields from the tower, U_b and V_b denote background winds, and U_l and V_l represent local winds.

A sea-land breeze day (SLBD) is defined as any 24 hours period exhibiting a distinct transition from sea breezes during the day to land breezes at night (Xiao et al., 2023). SLB identification criteria vary regionally due to differences in topography

https://doi.org/10.5194/egusphere-2025-3215
Preprint. Discussion started: 4 September 2025

and coastline geometry (Huang et al., 2025). For the NS station, located north of the Pearl River Estuary, sea breeze and land breeze directions are defined as 112–202° and 302–45°, respectively, based on local coastline features. Drawing from SLB criteria in Table S1 in the Supplement and historical SLB patterns in the Pearl River Estuary (Qiu and Fan, 2013b; Zhang et al., 2024; Mai et al., 2024b), the land breeze period is defined as 01:00–09:00, and the sea breeze period as 12:00–20:00. Guangzhou's SLBD identification rules are: (1) daily mean wind speed < 10 m s^{-1}; (2) local winds persistently meet land/sea breeze direction criteria for ≥ 4 hours within their respective periods, or (3) land/sea breeze directions occur for ≥ 4 hours within any 5-hour window of their respective periods. Otherwise, the day is designated a non-SLB day (NSLBD).

2.5 Estimation of CO_2tot, CO_2ff, and CO_2bio

The observed CO_2 concentration enhancements at tall-tower sites represent the integrated effect of upwind surface fluxes transported by atmospheric advection (Lin et al., 2003). Consequently, upwind carbon emissions can be inversely derived from site-specific enhancement measurements coupled with their corresponding atmospheric footprints. We employ a simplified methodology integrating observational data and atmospheric transport modeling to estimate total urban CO_2(CO_2tot) and CO (COtot) emissions. This approach operates independently of a priori emission inventories for the study region, requiring only: concentration enhancement observations at receptor sites, and simulated atmospheric footprints from transport models—consistent with prior regional flux quantifications of CO_2, CH_4, and CO (Mitchell et al., 2018; Lin et al., 2021; Wu et al., 2022a). CO_2tot and COtot are calculated as:

$$CO_2tot = \frac{CO_{2,s}obs - CO_2bg}{\sum_i Footprint_{i,s}}, \quad (8)$$

$$COtot = \frac{CO_s obs - CObg}{\sum_i Footprint_{i,s}}, \quad (9)$$

The numerators are hourly CO_2 and CO concentration enhancements (ΔCO_2 and ΔCO) at station s, where $CO_{2,s}$obs and CO_sobs represent observed CO_2 and CO concentrations, while CO_2bg and CObg denote urban background concentrations (detailed in the Supplement). The denominators are hourly total atmospheric footprints ($\sum_i \mathrm{Footprint}_{i,s}$), where i denotes backward particle release time from the receptor. Due to challenges in modeling mixed-layer depths during nighttime, morning, and evening, flux analysis focuses on afternoon hours (12:00–16:00) (Boon et al., 2016; Mitchell et al., 2018; Lin et al., 2021). Daily-scale CO_2tot and COtot are derived by dividing the mean afternoon ΔCO_2 and ΔCO by the corresponding mean $\sum_i \mathrm{Footprint}_{i,s}$, The footprint quantifies the sensitivity of concentration enhancements at the observation site to upwind surface fluxes, as detailed in Sect. 2.5.1. $\triangle CO_2$ is in units of [ppm], while footprint is in [ppm / (μmole m^{-2} s^{-1})], so CO_2tot, the quotient between the two quantities, is in flux units of [μmole m^{-2} s^{-1}].

Anthropogenic CO_2 emissions (CO_2ff) are derived from COtot and the CO/CO_2 emission ratio (R_{CO}), where R_{CO} is determined

https://doi.org/10.5194/egusphere-2025-3215
Preprint. Discussion started: 4 September 2025

from real-time tower-measured data, as described in detail in Sect. 3.4:

$$CO_2ff = \frac{COtot}{Rco}, \quad (10)$$

Biogenic fluxes (CO_2bio) are calculated as residuals:

$$CO_2bio = CO_2tot - CO_2ff. \quad (11)$$

Positive CO_2bio values indicate biogenic carbon emissions, while negative values denote carbon uptake, reflecting the dual role of urban biospheres as CO_2 sources and sinks (Kim et al., 2025).

2.5.1 Atmospheric transport model

To trace airmass sources entering the urban domain and reaching observation sites, and to assess CO_2 emissions corresponding to observed concentration enhancements, the Stochastic Time-Inverted Lagrangian Transport model (STILT-Rv2) was employed for atmospheric transport simulations, driven by meteorological fields from the Weather Research and Forecasting Model (WRFv4.1.1). In this study, STILT serves two purposes: (1) providing airmass trajectories for identifying marine background concentrations in Guangzhou, and (2) generating atmospheric footprints for quantifying total CO_2 and CO emissions.

The STILT model simulates atmospheric transport by releasing a set of air particles backward in time from the receptor location at the observation height. These particles are tracked spatially and temporally as they disperse upwind. The resulting trajectories delineate source regions influencing the receptor site and quantify the sensitivity of observed concentrations to upwind surface fluxes, termed "source-receptor relationships" or "atmospheric footprints" (Lin et al., 2003; Fasoli et al., 2018). Footprints represent the contribution of upwind sources/sinks to downwind concentration changes, with higher sensitivities near receptors or under stable wind conditions, where boundary layer airmasses interact more directly with surface fluxes (Wu et al., 2022a). For this study, 500 particles were released at 48 m (PY stations) heights, and traced backwards in time for 72 h. Footprints were computed at 0.08° × 0.08° spatial resolution. Periods with total footprint sensitivities ($\sum_i \mathrm{Footprint}_i$) below the 10th percentile were excluded, indicating low sensitivity to regional surface fluxes (Lin et al., 2021).

2.5.2 Uncertainty sources

Uncertainties associated with emission estimates derived from Eqs. (12)–(14) primarily arise from: (1) observational uncertainties, (2) background concentration uncertainties, (3) atmospheric transport uncertainties (footprints) and (4) R_{CO} uncertainties. Here, footprint uncertainties are neglected under the assumption of unbiased atmospheric transport during observations. The R_{CO} uncertainty originates from factors (1) and (2). Collectively, the dominant uncertainties in CO_2tot and

https://doi.org/10.5194/egusphere-2025-3215
Preprint. Discussion started: 4 September 2025

CO_2bio quantification stem from observational and background concentration errors, calculated as:

$$E_u^2 = OBS_{u,c}^2 + BG_u^2 , \quad (12)$$

where $OBS_{u,c}$ represents uncertainty in urban atmospheric observations, and BG_u represents uncertainty in urban background concentrations. We cannot accurately quantify all error sources involved in instrumental measurements; some minor error sources (e.g., uncertainty related to water vapor) may be negligible, while the primary uncertainty originates from discrepancies between measured the concentration of air samples and calibration standards (Verhulst et al., 2017). Here, $OBS_{u,c}$ is calculated as the standard deviation (SD) of residuals H (Yang et al., 2021). For urban background uncertainties:

$$BG_{u,co2}^2 = CT_{co2,r}^2 + CT_{co2,s}^2 , \quad (13)$$

$$BG_{u,co}^2 = OBS_{co,r}^2 + OBS_{co,s}^2 . \quad (14)$$

CO_2 background uncertainty ($BG_{u,co2}$) combines the absolute monthly smoothed residuals ($CT_{co2,r}$) and variability (SD) of monthly CO_2 concentrations ($CT_{co2,s}$) from Carbon Tracker (CT). Similarly, CO background uncertainty ($BG_{u,co}$) is derived from monthly smoothed residuals ($OBS_{co,r}$) and variability ($OBS_{co,s}$) of in situ observations.

3 Results and discussion

3.1 Spatiotemporal patterns of atmospheric CO_2

Figure 2 presents the hourly mean time series of atmospheric CO_2 concentrations at the NS, PY, and CH stations in Guangzhou from January 1, 2023, to September 30, 2024. To assess wind field impacts on CO_2 variability (Fig. S2), concentrations were classified into five categories: local (wind speed < 1.5 m s^{-1}) and four directional sectors (wind speed ≥ 1.5 m s^{-1}) defined as NE (0–90°), SE (90–180°), SW (180–270°), and NW (270–360°). All stations exhibited significant temporal variability, with standard deviations (SD) of 13.90 (NS), 15.92 (PY), and 16.05 ppm (CH), consistent with urban and suburban observations in Hangzhou, Beijing, Xi'an, and Seoul (Park et al., 2021; Yang et al., 2021; Chen et al., 2024; Liu et al., 2025). PY showed the highest CO_2 levels and variability, driven predominantly by local-type emissions under low wind speeds. In contrast, the NS coastal station exhibited elevated concentrations during northerly winds (NW/NE). Seasonal wind effects were pronounced: summer southerly winds (SW/SE) reduced CO_2 at PY and NS (most notably at NS near the coast), while winter northerly winds (NW/NE) increased CO_2 at NS.

https://doi.org/10.5194/egusphere-2025-3215
Preprint. Discussion started: 4 September 2025

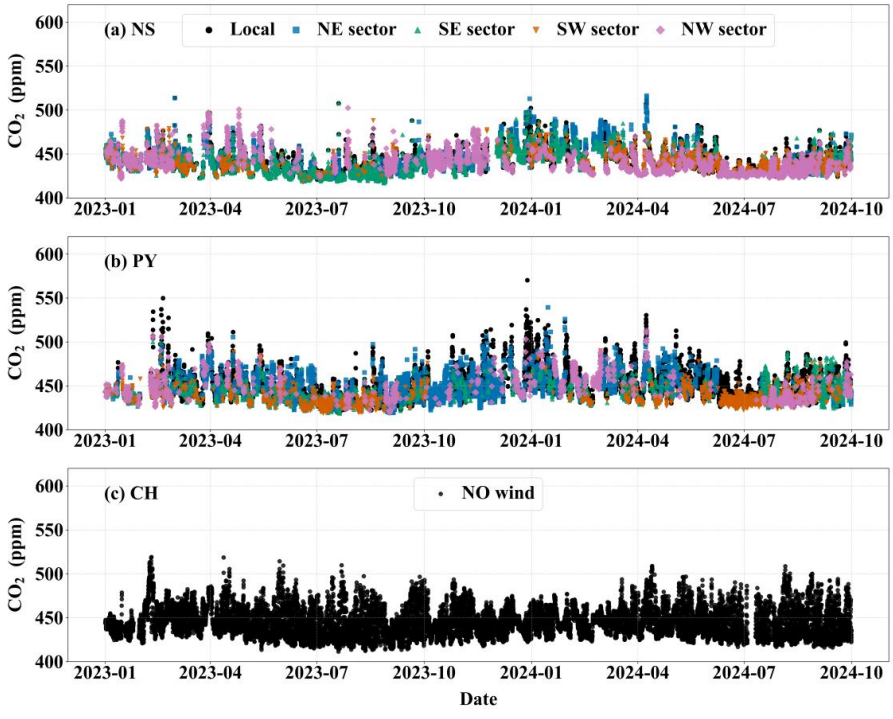

Figure 2. Time series of atmospheric CO_2 concentrations at the (a) NS, (b) PY, and (c) CH stations. For the NS and PY stations, data are color-coded by wind speed and direction, classified as either local (wind speed < 1.5 m s^{-1}) or one of four directional sectors (NE (0–90°), SE (90–180°), SW (180–270°), NW (270–360°)) for winds with speed ≥ 1.5 m s^{-1}.

Urban-rural CO_2 gradients vary globally due to differences in economic activity, population density, land use, and energy infrastructure, reflecting heterogeneous urban carbon emissions (Gao et al., 2022). In Guangzhou, mean CO_2 concentration differences between PY and NS/CH were 6.67 and 3.43 ppm, respectively, forming a distinct "urban dome" (urban > suburban > coastal). The NS-CH difference (3.44 ppm) highlights comparable gradients between suburban and coastal zones. This gradient mirrors Los Angeles's coastal megacity profile but with a smaller magnitude (Verhulst et al., 2017). Guangzhou's urban-suburban difference (3.43 ppm) aligns with Hangzhou's 2021 observations (4.96 ppm) (Chen et al., 2024) but is lower than Nanjing (8.1 ppm, 2014) and Beijing (12.4 ppm, 2018–2019) (Gao et al., 2018; Yang et al., 2021). It remains far smaller than Shanghai (55.1 ppm, 2014) and Baltimore (66.0 ppm, 2002–2006) (Pan et al., 2016; George et al., 2007). Over time, urban emissions may stabilize as suburban populations and fossil fuel demand grow, potentially narrowing urban-suburban CO_2 differences (Mitchell et al., 2018). For instance, Hangzhou's reduced gradient reflects urbanization-driven energy consumption, where suburban monitoring captures urban emission influences (Chen et al., 2024).

3.1.1 Seasonal variability of atmospheric CO_2

Figure 3 illustrates the monthly mean variations in atmospheric CO_2 concentrations at the NS, PY, and CH stations in

https://doi.org/10.5194/egusphere-2025-3215
Preprint. Discussion started: 4 September 2025

Guangzhou, alongside their correlations with the Normalized Difference Vegetation Index (NDVI). NDVI data at 1 km × 1 km spatial resolution were obtained from NASA's EOSDIS Land Processes Distributed Active Archive Center (Didan, 2015), with values within a 3-km radius buffer around each station center used for comparative analysis. All three stations exhibited consistent seasonal CO_2 patterns, with higher concentrations in winter/spring and lower values in summer/autumn, mirroring observations in Hangzhou (Chen et al., 2024). These variations arise from the combined effects of (1) seasonal biogenic flux cycles, (2) anthropogenic emission variability, and (3) boundary layer height dynamics (Xueref-Remy et al., 2018). Enhanced vegetation photosynthesis during warmer months (summer/autumn, Table S2 in the Supplement) strengthens biogenic carbon sinks, while higher boundary layer depths (Fig. S6 in the supplement) and southerly marine air masses (Fig. 2) promote atmospheric mixing and CO_2 dispersion.

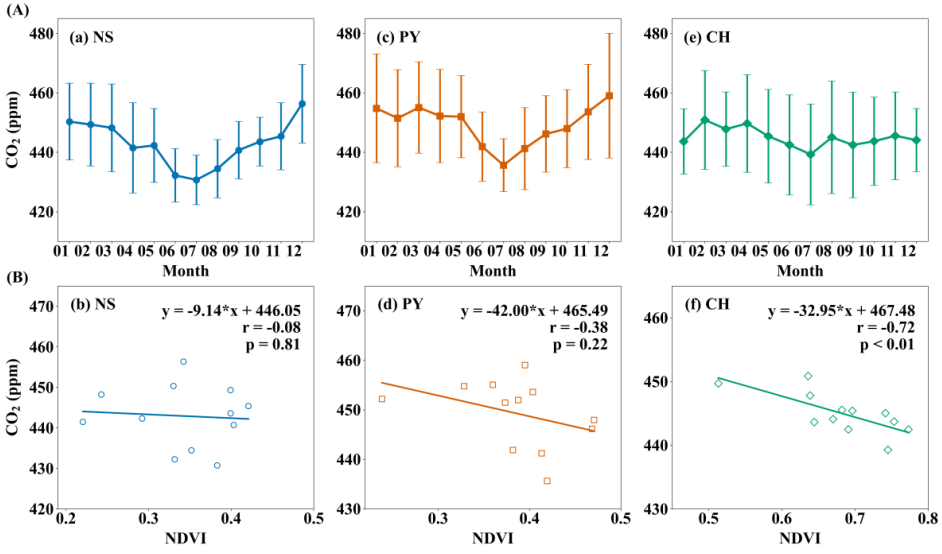

Figure 3. (A) Variations in monthly mean CO_2 concentrations and (B) their correlations with Normalized Difference Vegetation Index (NDVI) for the (a–b) NS, (c–d) PY, and (e–f) CH stations. Error bars indicate ± 1 standard deviation (SD).

The amplitudes of the seasonal variation of CO_2 at NS, PY, and NS are 25.63, 23.38, and 11.59 ppm, respectively. NS and PY peaked in December and troughed in July, whereas CH peaked in February and troughed in July. NS's large amplitude reflects its extreme December highs and July lows. In December, prevailing northerly winds (Figs. 2a and S2a) transported urban emissions to downwind NS, narrowing its CO_2 difference with PY to 2.68 ppm. Conversely, July saw NS's CO_2 concentrations fall to the lowest among all stations—4.93 ppm and 8.56 ppm below PY and CH, respectively—establishing a south-to-north increasing gradient (coastal < urban < suburban). This gradient aligns with marine-influenced southerly air masses, which dilute coastal CO_2 while transporting urban emissions northward, potentially accumulating CO_2 in northern suburbs.

Despite CH's stronger biogenic coupling (NDVI correlation: −0.72; Fig. 3f), NS's CO_2 levels remained 9.80 ppm lower than

https://doi.org/10.5194/egusphere-2025-3215
Preprint. Discussion started: 4 September 2025

CH in summer and 5.80 ppm higher in winter, underscoring transport-dominated over biogenic controls at the coastal site. NS's weak NDVI correlation (−0.08) and low NDVI range (0.22–0.42) further support minimal biogenic influence. Additionally, deeper summer boundary layers at NS and PY (Fig. S6) enhanced vertical CO_2 dispersion. In February, CH recorded its annual CO_2 maximum, driven by vegetation respiration during early growth stages and elevated emissions from fireworks around the Lunar New Year, as CH's location falls outside Guangzhou's fireworks restriction zones (https://www.gz.gov.cn/gfxwj/qjgfxwj/chq/qf/content/post_7198980.html, last access: 18 June 2025). This finding is corroborated by CO observations: CH's CO concentrations peaked in February due to firework emissions, whereas other sites peaked in December (Fig. S7 in the Supplement).

3.1.2 Diurnal variations of atmospheric CO_2

The diurnal patterns of atmospheric CO_2 concentrations at NS, PY, and CH stations in Guangzhou consistently exhibited lower daytime and higher nighttime values (Fig. 4). This is attributed to the shallow nocturnal boundary layer, which traps anthropogenic and biogenic emissions near the surface, elevating CO_2 levels. After sunrise, surface heating deepens the boundary layer, diluting surface emissions and entraining free tropospheric air with lower CO_2 concentrations. Concurrently, daytime photosynthetic uptake further reduces near-surface CO_2 (Mitchell et al., 2018). We further evaluate urban-suburban-coastal differences in these processes. At PY, the CO_2 peak occurred at 08:00–09:00, aligning with morning traffic peaks, reflecting dominant anthropogenic influences. CH's peak appeared 1–2 hours earlier than PY due to its longitudinal and elevational position, where earlier sunrise accelerates the breakup of the nocturnal stable boundary layer. Both PY and CH reached minima at 16:00–17:00, likely linked to afternoon photosynthetic activity. NS exhibited irregular peak/valley timing.

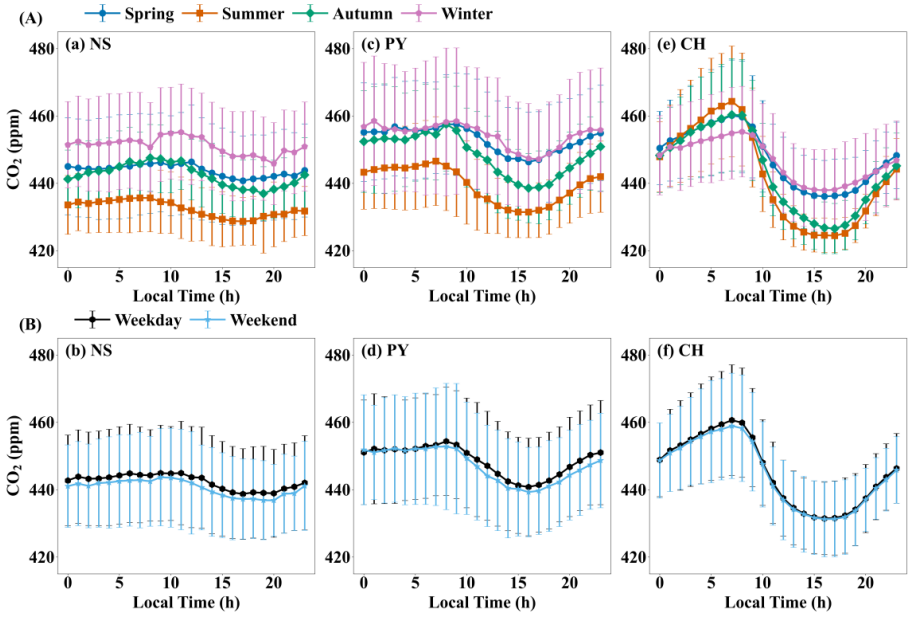

https://doi.org/10.5194/egusphere-2025-3215
Preprint. Discussion started: 4 September 2025

Figure 4. Diurnal CO_2 variations at the (a–b) NS, (c–d) PY, and (e–f) CH stations across (A) seasons and (B) weekdays/weekends. Seasons are defined as spring (Mar–May), summer (Jun–Aug), autumn (Sep–Nov), and winter (Dec–Feb). Error bars indicate ± 1 SD.

Diurnal amplitudes at CH and PY were larger in summer/autumn than winter/spring, driven by vegetation activity and boundary layer dynamics (Fig. S8 in the Supplement). Summer/autumn conditions in Guangzhou—abundant light, warmth, and rainfall—optimize vegetation growth, enhancing daytime photosynthesis and nighttime respiration (Dusenge et al., 2019). Optimal canopy temperatures for subtropical evergreen forests (~30 °C) (Liu et al., 2015) align with CH/PY's summer/autumn daytime temperatures (Table S2), explaining their amplified amplitudes. However, the diurnal amplitude of CO_2 at CH in summer and autumn is 2.63 times and 1.77 times that at PY, respectively. The diurnal amplitude of atmospheric CO_2 concentration at CH in summer is 39.90 ppm, which is close to the diurnal amplitude of CO_2 concentration in the suburbs of Hangzhou in summer (35.29 ppm)(Chen et al., 2024). Despite similar temperatures, CH's larger NDVI range and stronger NDVI-CO_2 correlation (−0.72 vs. PY; Figs. 3d and f) highlight greater biogenic dominance, with pronounced daytime uptake and nighttime respiration. NS showed the smallest diurnal amplitudes across seasons (e.g., 5.60 ppm in summer), attributable to sparse vegetation (low NDVI: 0.22–0.42) and frequent summer southerly marine air masses, which dilute coastal CO_2.

Figure 4B contrasts weekday-weekend diurnal CO_2 patterns. All stations showed higher weekday concentrations, diverging from Hangzhou and Beijing (Yang et al., 2021; Chen et al., 2024) but aligning with Paris and Boston (Briber et al., 2013; Xueref-Remy et al., 2018). At CH, smaller daytime weekday-weekend differences suggest biogenic fluxes outweigh anthropogenic variations. At PY, reduced weekend traffic (central urban location) drove daytime declines. NS's persistently higher weekday CO_2 reflects construction activities (e.g., Metro Line 18 extension) and weekday-intensive port operations (e.g., Nansha Container Terminal Phase III, 5 km east), which maintain 24/7 workflows (e.g., Shanghai Port's daily operational indices: http://sisi-smu.org/2025/0422/c12041a243211/page.htm, last access: 18 June 2025).

3.2 Sea-land breeze impacts

Based on meteorological observations from the NS coastal tall tower, 84 sea-land breeze days (SLBD) were identified in Guangzhou between January 2023 and September 2024, accounting for 13.14 % of the monitoring period, with peaks in spring and autumn. These transitional seasons between summer and winter are characterized by weaker synoptic systems and lighter background winds, favoring SLBD occurrence (Mai et al., 2024b). Our results align with SLBD seasonal distributions for the Pearl River Estuary cities of Zhuhai and Guangzhou in 2022 (Zhang et al., 2024; Mai et al., 2024b). Figure 5 compares CO_2 concentrations during SLBD and non-SLB days (NSLBD) across stations. Overall, average CO_2 concentrations during SLBD were 5.87 ppm (NS), 3.08 ppm (PY), and 0.75 ppm (CH) lower than during NSLBD, indicating that sea-land breeze (SLB) circulation enhances CO_2 dispersion, with coastal > urban > suburban impacts, similar to SLB-driven $PM_{2.5}$, PM_{10}, and ozone

https://doi.org/10.5194/egusphere-2025-3215
Preprint. Discussion started: 4 September 2025

dispersion patterns in Tianjin (Hao et al., 2017). Seasonal differences were pronounced: SLB promoted CO_2 dispersion at NS and PY in spring, winter, and autumn (spring > winter > autumn), but increased CO_2 accumulation in summer. Tianjin similarly observed summer $PM_{2.5}/PM_{10}$ accumulation under SLB (Hao et al., 2017). At CH, SLBD reduced CO_2 in spring, summer, and autumn but increased it in winter, likely due to limited inland SLB penetration and competing winter processes.

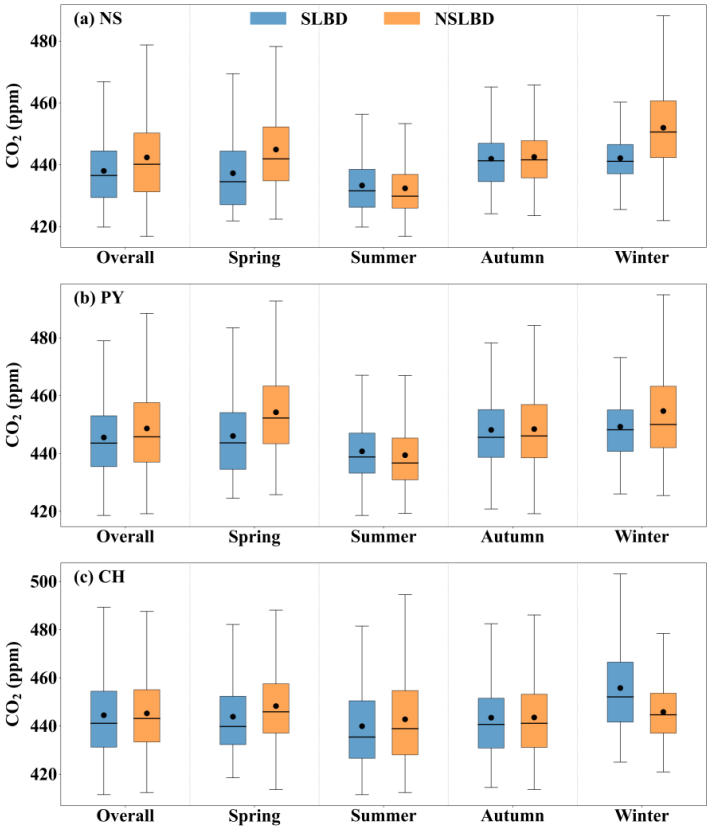

Figure 5. Boxplots of atmospheric CO_2 concentrations (black dots denote means) during sea-land breeze days (SLBD) and non-SLB days (NSLBD) by station and season, with outliers excluded.

To resolve seasonal and diurnal SLB impacts, we analyzed CO_2 diurnal variations during SLBD and NSLBD (Fig. 6). Focusing on NS (due to similar PY-NS trends and space constraints), spring and winter SLBD reduced CO_2 concentrations by 7.76 ppm and 9.77 ppm (hourly mean differences), respectively, driven by stronger winds (Fig. 6) and deeper boundary layers (Fig. S9 in the Supplement). Autumn SLB only reduced CO_2 during sea breeze hours (mean difference: 1.69 ppm). Autumn's weaker winds and boundary layers resulted in reduced dispersion compared to spring/winter. In summer, SLB increased CO_2 by 2.08 ppm (sea breeze hours) due to stable atmospheric stratification. Summer temperatures were 6.00 °C and 12.19 °C higher than spring and winter (Table S2), respectively. Under calm, rain-free conditions, the collision of moist marine air with dry-hot coastal land formed a thermal internal boundary layer (TIBL), inducing low-level temperature inversions near the SLB

https://doi.org/10.5194/egusphere-2025-3215
Preprint. Discussion started: 4 September 2025

353 convergence zone (Liu et al., 2001; Reddy et al., 2021). These inversions suppressed horizontal/vertical mixing, trapping CO_2
354 (Stauffer et al., 2015; Hao et al., 2024). NS's summer SLBD winds averaged 1.05 m s^{-1} (sea breeze) and 0.96 m s^{-1} (land
355 breeze)—38.60 %, 63.16 %, and 15.32 % lower than spring, winter, and autumn winds, respectively—while boundary layer
356 heights (590.54 m) were 9.51 % shallower than NSLBD (Fig. S9). Weak winds and shallow boundary layers stabilized
357 atmospheric stratification, limiting CO_2 dispersion and elevating ground-level CO_2 by up to 4.03 ppm.

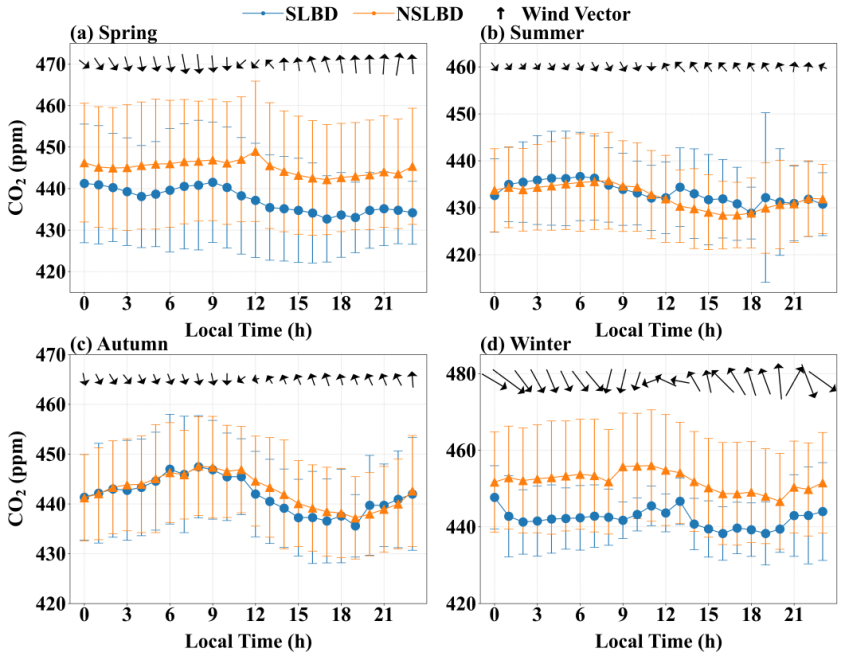

358

359 **Figure 6.** Diurnal variations in CO_2 concentrations, wind direction, and wind speed at the coastal station (NS) during sea-land breeze
360 days (SLBD) and non-SLB days (NSLBD) by season. Error bars indicate ± 1 SD.

361 **3.3 CO_2 enhancements and uncertainties**

362 Figure S10 (in the Supplement) presents the time series of observed CO_2 and CO concentrations at Guangzhou's stations
363 relative to marine backgrounds from January 1 to December 27, 2023. Compared to urban observations with significant hourly
364 variability, marine background concentrations in Guangzhou remained stable, with summer and winter CO_2 standard deviations
365 of 0.94 ppm and 0.67 ppm, respectively, indicating minimal local source/sink influences. Using Eqs. (13) and (14), marine
366 background uncertainties were calculated (Table S3 in the Supplement). Summer and winter CO_2 marine background
367 uncertainties were 0.96 ppm and 0.70 ppm, respectively, constraining urban marine background uncertainties below 1 ppm—
368 slightly lower than Los Angeles's 1.4 ppm (Verhulst et al., 2017). CO marine background uncertainties were 12.68 ppb
369 (summer) and 18.36 ppb (winter).

370

https://doi.org/10.5194/egusphere-2025-3215
Preprint. Discussion started: 4 September 2025

Based on marine backgrounds, CO_2 enhancements were derived for all stations. Figure 7 shows enhancements across all hours, afternoon (12:00–16:00), and midnight (00:00–05:00) periods in 2023, summer, and winter. Annual median enhancements were 13.59 (NS), 17.70 (PY), and 16.29 ppm (CH), with pronounced spatiotemporal variability—closely aligning with the 10–20 ppm range observed annually in the Beijing-Tianjin-Hebei (BTH) urban cluster of China (Han et al., 2024). In summer, enhancements followed a south-to-north gradient: 7.00 (NS), 13.23 (PY), and 16.91 ppm (CH). Afternoon enhancements peaked at PY (6.92 ppm), critical for emission inversion, while midnight enhancements at CH reached 31.36 ppm—1.85 times and 3.43 times higher than PY and NS. Winter afternoon enhancements reversed this pattern: 16.58 (NS), 12.37 (PY), and 7.45 ppm (CH), with NS and PY values 4.39 times and 1.79 times higher than summer. Midnight enhancements at CH remained highest in winter (18.87 ppm), despite a 38.93 % reduction from summer.

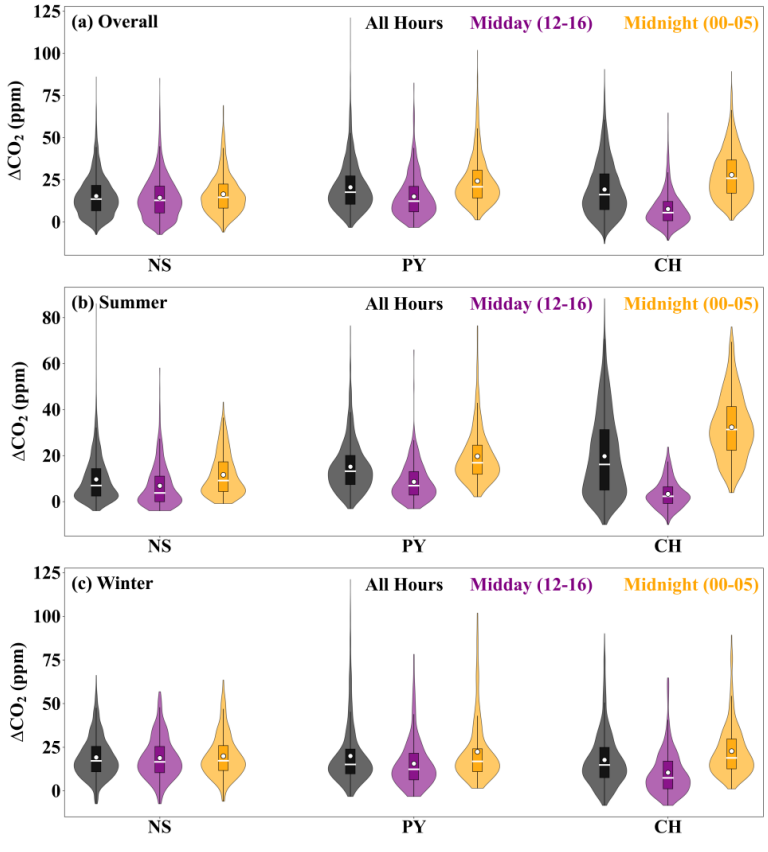

Figure 7. Hourly CO_2 enhancement above the marine background level at each station during the (a) overall, (b) summer, and (c) winter periods. The white dots represent the mean values.

This spatiotemporal variability reflects divergent influences of anthropogenic emissions, biogenic fluxes, and atmospheric mixing. At CH, strong diurnal shifts in enhancements (e.g., 31.36 ppm summer midnight) highlight biogenic dominance, with long-tailed distributions (Fig. 7). Stable, shallow nighttime boundary layers trapped respiratory emissions near the surface,

https://doi.org/10.5194/egusphere-2025-3215
Preprint. Discussion started: 4 September 2025

consistent with isotopic studies in Xi'an (32.80 ppm) and Switzerland (30.00 ppm) (Wang et al., 2021; Berhanu et al., 2017). At NS, transport dominated: summer southerly marine air masses reduced enhancements, while winter northerly winds transported urban emissions downstream, raising NS enhancements to PY levels (exceeding PY in afternoons). PY's enhancements were primarily anthropogenic, validated by CO co-variation. CO, a tracer for combustion-derived CO_2 (Newman et al., 2013; Che et al., 2022), showed significantly higher concentrations at PY (Fig. S10). PY's median midnight CO enhancements in summer were 2.04 times and 1.43 times higher than NS and CH (Fig. S11 in the Supplement). Shallow nocturnal boundary layers localized anthropogenic CO near the surface, with minimal vertical/horizontal transport, confirming PY's anthropogenic dominance.

3.4 Continuous observations of $\Delta CO/\Delta CO_2$ ratios

Reduced Major Axis regression (Model II) was applied to analyze the relationship between CO (ΔCO) and CO_2 (ΔCO_2) concentration enhancements across stations, with the $\Delta CO/\Delta CO_2$ ratio (R_{CO}) derived from regression slopes (Fig. 8). In 2023, R_{CO} values for NS, PY, and CH were 8.48 ± 1.81, 7.45 ± 1.38, and 4.16 ± 3.59 ppb ppm^{-1}, respectively, with correlation coefficients of 0.78, 0.72, and 0.33, indicating significant spatiotemporal heterogeneity. Summer R_{CO} was generally lower than winter, with CH exhibiting the lowest seasonal value (2.66 ± 0.83 ppb ppm^{-1}). Winter maxima occurred at NS (11.03 ± 1.49 ppb ppm^{-1}), followed by PY (9.08 ± 1.13 ppb ppm^{-1}) and CH (8.56 ± 1.82 ppb ppm^{-1}).

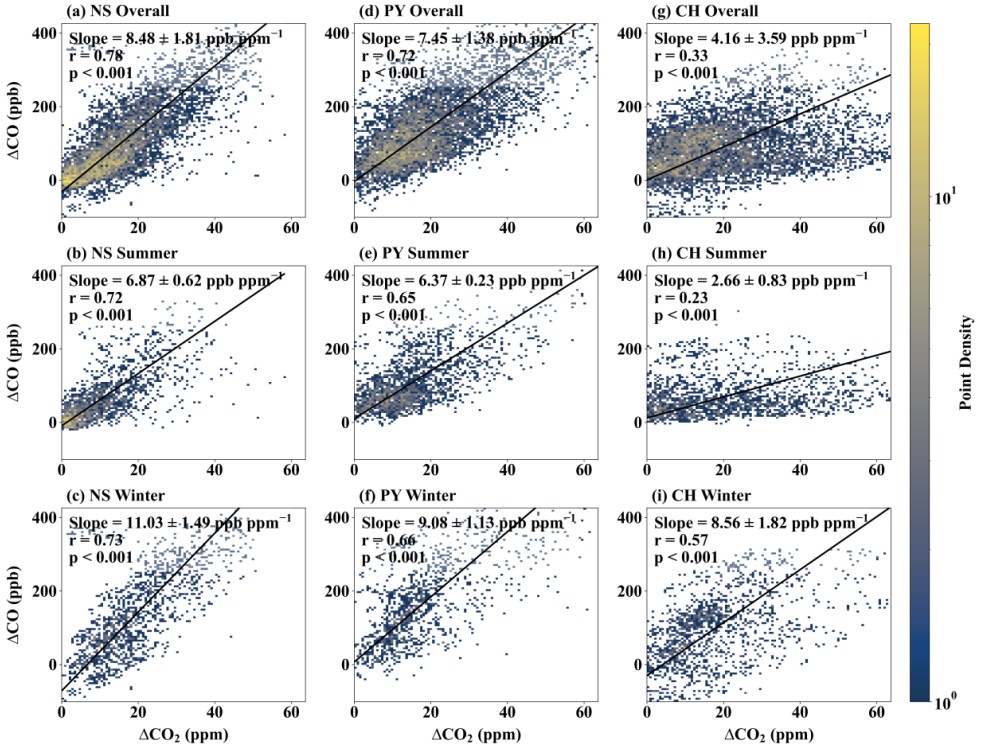

Figure 8. Relationships between ΔCO_2 and ΔCO concentration enhancements analyzed by geometric mean regression for different

https://doi.org/10.5194/egusphere-2025-3215
Preprint. Discussion started: 4 September 2025

seasons at the (a–c) NS, (d–f) PY, and (g–i) CH stations, where the slope values represent the $\Delta CO/\Delta CO_2$ ratios (R_{CO}).

Comparatively, Beijing's urban R_{CO} in 2019 was measured at 10.46 ± 0.11 ppb ppm^{-1} using portable Fourier-transform spectroscopy (Che et al., 2022), while Shanghai and Los Angeles showed 10.22 ± 0.40 and 9.64 ± 0.46 ppb ppm^{-1}, respectively, based on satellite and model data (Wu et al., 2022a). Guangzhou's lower R_{CO} reflects improved combustion efficiency driven by stringent post-2013 air quality policies. For example, Beijing's R_{CO} dropped from > 30 ppb ppm^{-1} in 2006 (Han et al., 2009) to 10.22 ± 0.40 ppb ppm^{-1} by 2020 (Wu et al., 2022a), with similar declines during the 2008 Olympics and 2020 COVID-19 lockdowns (Wang et al., 2010; Cai et al., 2021). In Guangdong, policies restricting coal plants, retiring inefficient industries, and promoting electric vehicles further enhanced combustion efficiency. For instance, attributed to strict air pollution controls, SO_2 and NO_2 levels in this region decreased by 85 % and 35 % respectively in 2019 compared to 2006 (Hu et al., 2021), demonstrating improved fossil fuel combustion efficiency. Mai et al. (2021) also reported the combustion efficiency improvement in the Pearl River Delta region due to technological advancements in gasoline vehicles.

Seasonal R_{CO} variations stem from biogenic flux and transport dynamics. Summer's weaker ΔCO-ΔCO_2 correlations at CH (Fig. 3B) reflect dominant biogenic influences (daytime uptake and nighttime respiration), as reported in Beijing, Indianapolis, and Switzerland (Turnbull et al., 2015; Berhanu et al., 2017; Che et al., 2022). Biogenic impacts decreased from suburban > urban > coastal, aligning with vegetation gradients. Winter's higher R_{CO} at CH and NS correlated with reduced biogenic activity and northerly transport of urban emissions under stable boundary layers. Berhanu et al. (2017) attributed winter R_{CO} increases to cold-air advection and boundary layer accumulation. NS's winter R_{CO} (4.16 ppb ppm^{-1} higher than summer) linked to urban airmass origins, while PY's seasonal shifts reflected suburban source-sink variations. Although secondary CO from upwind Volatile Organic Compounds (VOCs) and CH_4 oxidation could perturb R_{CO}, their combined contribution was merely 1 % in coastal urban regions (Griffin et al., 2007).

3.5 Partitioning anthropogenic and biogenic fluxes

Given the CH station's heightened sensitivity to biogenic fluxes—particularly during summer when its R_{CO} incorporates more pronounced biogenic components—contrasted with NS station's dominant atmospheric transport influences (especially winter R_{CO} perturbations from upwind urban emissions), PY station was selected to quantify total CO_2 emissions (CO_2tot) driving observed concentration enhancements. Utilizing site-specific R_{CO} measurements, CO_2tot was partitioned into fossil-derived CO_2 (CO_2ff) and biogenic CO_2 (CO_2bio).

Fig. 9 displays mean CO_2tot, CO_2ff, and CO_2bio at PY station during summer and winter afternoons (12:00–16:00), with error bars denoting seasonal standard deviations. Persistent dominance of CO_2ff over CO_2bio underscores anthropogenic control of

https://doi.org/10.5194/egusphere-2025-3215
Preprint. Discussion started: 4 September 2025

urban CO_2 emissions—a pattern corroborated in Chinese cities like Beijing (65 ± 3 %) and Xi'an (82 ± 2 %) where fossil fuels dominate observed enhancements (Wang et al., 2022). Elevated winter (December) CO_2ff relative to summer (July) primarily reflects atmospheric dynamics dominating summertime dilution: marine air mass advection and boundary layer changes suppressed summer enhancements to merely 20 % of winter levels despite a 19 % larger summer footprint (Figs. 7 and S3). The seasonal contrast was secondarily modulated by anthropogenic factors, notably natural gas consumption surges for heating and holiday cooking during Lunar New Year/New Year festivities. This seasonal trend parallels Los Angeles' fossil fuel minima in July–September and maxima in December–March (Kim et al., 2025), with analogous cold-season amplification documented in Indianapolis eddy flux observations (Wu et al., 2022b). Notably, summer CO_2bio at PY exceeded winter levels, aligning with NDVI seasonality (summer NDVI was 11 % higher than winter) and contrasting temperatures: summer averaged 30.21 °C, near the optimal canopy temperature for photosynthesis (Liu et al., 2015), while winter was considerably cooler at 17.38 °C (Table S2). Summer afternoons revealed biogenic fluxes offsetting 60.17 % of anthropogenic emissions—highlighting critical biogenic modulation of coastal urban carbon budgets. This magnitude resonates with Los Angeles' growing-season biogenic consumption of 60 % fossil emissions (Kim et al., 2025), while New York City's summer biogenic uptake offsets 40 % of anthropogenic enhancements, fully neutralizing traffic emissions in highly congested zones (Wei et al., 2022). Crucially, data from Indianapolis demonstrating equivalent warm-season amplitudes between CO_2bio and CO_2ff underscore the necessity of accounting for biogenic fluxes in urban CO_2ff quantification (Wu et al., 2022b).

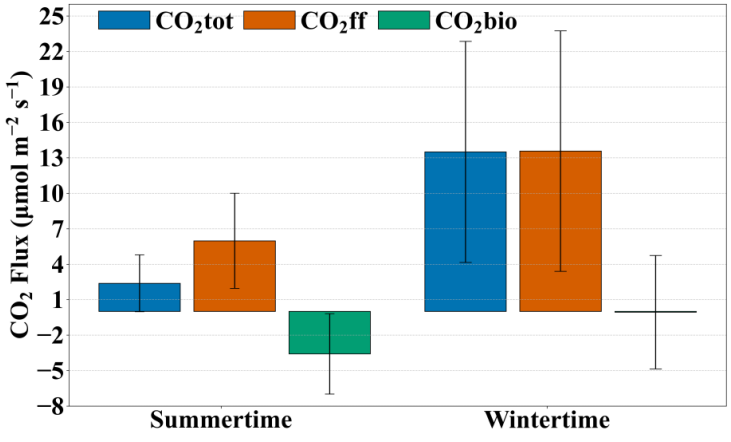

Figure 9. Average CO_2tot, CO_2ff, and CO_2bio derived from CO_2 enhancement observations at the PY station, during summer and winter afternoon hours (12:00–16:00). Error bars indicate ±1 SD.

The maximum winter afternoon CO_2ff at Guangzhou's urban site reached 13.62 ± 9.38 μmole m^{-2} s^{-1}. While uncertainties from in situ observations and background concentrations alone would yield a marginal flux error of 0.36 μmole m^{-2} s^{-1}, atmospheric transport introduces substantial unquantified uncertainty—consistent with documented winter wind speed overestimations in meteorological models (Yadav et al., 2021) and biases in simulating boundary layer-free troposphere

https://doi.org/10.5194/egusphere-2025-3215
Preprint. Discussion started: 4 September 2025

exchange (Lin et al., 2021). Though transport uncertainty quantification falls beyond this study's scope, we identified surface flux sensitivity zones via winter footprint distributions in Fig. 10 (bounded areas), where influence peaks near receptor sites (Wu et al., 2022). Temporally resolved EDGAR emissions within these sensitivity zones yielded a bottom-up CO_2ff estimate of 19.81 μmole m^{-2} s^{-1}. Our observation-model-R_{CO} derived CO_2ff (13.62 μmole m^{-2} s^{-1}) showed reasonable convergence despite a 6.19 μmole m^{-2} s^{-1} discrepancy—primarily attributable to transport uncertainties, paralleling the 3.5 μmole m^{-2} s^{-1} gap in Los Angeles attributed to mixed-layer height and wind speed errors (Kim et al., 2025). Summer afternoons exhibited peak CO_2bio of −3.67 ± 3.48 μmol m^{-2} s^{-1}. This aligns with the modeled Pearl River Delta net ecosystem exchange (NEE) range of −0.1 to −12 μmol m^{-2} s^{-1} (Mai et al., 2024a), U.S. urban observations such as Los Angeles with −6.7 ± 0.7 μmol m^{-2} s^{-1}, and broader reported biogenic flux ranges of 0 to −15 μmol m^{-2} s^{-1} (Wu et al., 2021; Wei et al., 2022; Kim et al., 2025). Crucially, bottom-up inventories proved inherently ill-equipped to resolve summer CO_2ff variability due to their statistical nature—exhibiting reductions in summer versus winter that were significantly smaller than observationally derived quantifications, at merely a quarter of the latter—and their inability to capture coastal atmospheric dynamics. This fundamental limitation, therefore, underscores the critical value of real-time monitoring for urban carbon flux assessment.

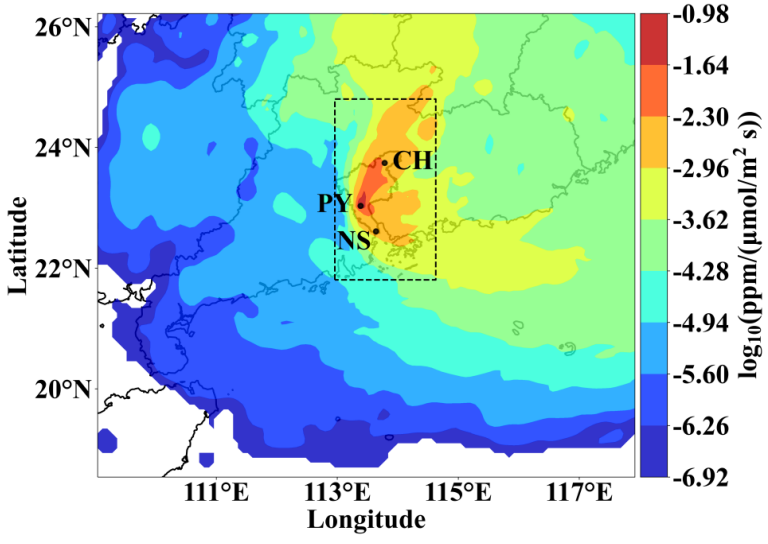

Figure 10. Spatial distribution of winter afternoon footprints at the PY station, highlighting high-sensitivity surface flux regions.

4 Conclusions

This study develops a novel observation-based framework that integrates high-precision atmospheric CO_2 measurements, meteorological analyses, and $\Delta CO/\Delta CO_2$ ratios (Rco) to disentangle the key drivers of CO_2 dynamics in the coastal megacity of Guangzhou. The analysis, covering the period from January 2023 to September 2024, successfully quantifies the respective roles of anthropogenic emissions, biogenic fluxes, and meteorological processes. The results demonstrate distinct regional

https://doi.org/10.5194/egusphere-2025-3215
Preprint. Discussion started: 4 September 2025

drivers of CO_2 variability: atmospheric transport dominates the large seasonal amplitude (25.63 ppm) at the coastal site, biogenic fluxes drive substantial diurnal cycles in suburban areas (peak summer amplitude: 39.90 ppm), and anthropogenic emissions exert primary control in the urban core. Notably, sea-land breeze (SLB), typically regarded as a ventilation mechanism, are found to amplify afternoon CO_2 accumulation by +2.08 ppm during summer under stable boundary layer conditions. During the peak growing season, urban biogenic fluxes offset 60.17 % of anthropogenic CO_2 emissions. Spatially heterogeneous Rco values, including an urban regression slope of 7.45 ± 1.38 ppb ppm^{-1}, confirm trends toward improved combustion efficiency.

The synthesis of these findings underscores that the CO_2 budget of a coastal megacity is governed by complex, non-linear interactions among emission sources, biospheric activity, and both synoptic and local meteorology. Our framework effectively partitions anthropogenic and biogenic contributions, revealing that biogenic fluxes are not merely a background signal but a dynamic and decisive component of the urban carbon cycle. Crucially, coastal meteorology exhibits a dual role: while SLB often facilitate ventilation, they can also trap and recirculate pollutants, leading to unanticipated CO_2 accumulation under specific atmospheric stratification.

Compared to existing studies, our innovative contributions to the current body of knowledge are as follows: (1) While prior research has largely overlooked the quantitative assessment of biogenic fluxes and their contribution to urban-scale CO_2 budgets, our study demonstrates that biogenic fluxes can offset up to 60.17 % of anthropogenic emissions during the peak growing season in a coastal megacity. This highlights the critical role of biogenic processes in urban carbon dynamics and overall CO_2 budgeting, underscoring the necessity of accurately accounting for these fluxes in future fossil fuel inversion studies. This finding helps address the gap in observational constraints and contribution assessments of biogenic fluxes in urban carbon cycle research. (2) Although the influence of SLB on urban CO_2 dynamics remains underexplored in existing literature, our work reveals a non-linear response of CO_2 to SLB, which can exacerbate CO_2 accumulation under stable boundary layer conditions—a critical feedback mechanism previously overlooked in urban carbon assessments. These results fill a fundamental knowledge gap regarding how CO_2 dynamics respond to SLB within coastal urban carbon cycle science. (3) The summer discrepancies between our observed CO_2ff and the bottom-up inventory suggest that such inventories struggle to capture the high-frequency variability induced by coastal atmospheric dynamics, an aspect that has been poorly documented in earlier work.

Despite validation against inventories, the NDVI, and independent studies confirming the robustness of our framework, several limitations remain. First, the spatial resolution of our three-station network limits the ability to resolve hyperlocal emission sources, such as individual traffic corridors. Second, gaps in high-resolution meteorological data, particularly in the suburban area, constrain a more comprehensive analysis of biosphere-weather interactions. Moreover, our identification of SLB events relies on 2D wind fields and does not incorporate full 3D boundary layer structures; however, the consistency of

https://doi.org/10.5194/egusphere-2025-3215
Preprint. Discussion started: 4 September 2025

our SLB identification with previous studies in the Pearl River Delta urban agglomeration suggests that this limitation does not significantly affect the core findings. Additionally, the derivation of biogenic fluxes as a residual of the CO_2 budget propagates uncertainties associated with the Rco tracer ratio and neglects minor contributions from secondary CO formation (< 1 %). Although beyond the scope of this study, uncertainties in atmospheric transport simulations remain a major factor contributing to flux estimation discrepancies. These limitations outline a clear pathway for future work, including the deployment of dense low-cost sensor networks, refinement of Rco estimates using VOC-based proxies, development of uncertainty-quantified coastal boundary layer models, and vegetation-specific flux measurements with isotopic constraints.

We show that coastal meteorology can override fundamental emission patterns, offering new insights into atmospheric CO_2 dynamics and emission inversion in coastal cities. These findings help reduce uncertainties in CO_2 inversion estimates across such regions. At the same time, rising atmospheric CO_2 levels—a major driver of global warming—intensify land-sea thermal contrast along coastlines, leading to more frequent sea-land breeze events. We further reveal that these breezes significantly influence coastal CO_2 dynamics. Consequently, the complex interactions and feedback mechanisms between sea-land breezes and CO_2 merit in-depth investigation in coastal atmospheric science. Moreover, by quantifying the substantial offset of anthropogenic CO_2 emissions by biogenic fluxes, our results underscore the need for high-resolution models of urban biogenic fluxes. This can be achieved through the installation of additional urban flux towers, improved constraints on CO_2 fluxes from urban lawns and mixed vegetation, and enhanced empirical parameterizations for biosphere models in urban settings. This work provides a scientific basis for urban policymakers to promote integrated gray-green infrastructure and harness ecological processes for climate mitigation. Finally, the methodology presented here—including the confirmed decline in urban combustion efficiency in response to policy interventions—can be extended to other cities to evaluate the effectiveness of climate mitigation strategies.

Code and data availability. The STILT model source code used in this paper has been published on Zenodo and can be accessed at https://doi.org/10.5281/zenodo.1196561 (Fasoli, 2018). The EDGAR data used in this study are publicly available at https://edgar.jrc.ec.europa.eu/dataset_ghg2024#conditions (last access: 18 June 2025)(Crippa et al., 2024). The planetary boundary layer height data used in this study are available at https://doi.org/10.24381/cds.adbb2d47 (Hersbach, 2023). The NDVI data used in this study are available at https://doi.org/10.5067/MODIS/MOD13A3.006 (Didan, 2015). The CarbonTracker (CT-NRT.v2024-5) products are available online at https://doi.org/10.15138/ATPD-K925 (Jacobson et al., 2024). The NOAA Earth System Research Laboratory/Global Monitoring Laboratory (NOAA GML) data used in this study are available at https://doi.org/10.25925/20241101 (Schuldt et al., 2024). Additional data and information used in this study are available from the corresponding author upon request.

Author contributions. JWZ and ML designed the study. JWZ, YJL, CLP, BH, YYH, XFL, SJS, CLC, CW, ZZ, JJL and ML contributed to data collection and data analysis. JWZ designed and performed the model simulations. JWZ and ML wrote the paper with contributions from all coauthors. JJL and SJS provided valuable feedback and opinions for paper refinement. All the authors revised the paper and edited the text.

https://doi.org/10.5194/egusphere-2025-3215
Preprint. Discussion started: 4 September 2025

Competing interests. The contact author has declared that none of the authors has any competing interests.

Acknowledgements. The authors would like to thank the personnel who participated in data collection, instrument maintenance, and logistic support during the field campaign. We also acknowledge the NOAA GML for providing the CO_2 GLOBALVIEWplus v10.1 ObsPack and CarbonTracker CT-NRT.v2024-5 datasets, which were used for monitoring comparison in this study. CarbonTracker CT-NRT.v2024-5 results provided by NOAA GML, Boulder, Colorado, USA from the website at http://carbontracker.noaa.gov.

Financial support. This work was financially supported by the National Natural Science Foundation of China (Grant no. 42477273) and the National Key R&D Program of China (Grant no. 2022YFE0209500).

References

Ahmadov, R., Gerbig, C., Kretschmer, R., Koerner, S., Neininger, B., Dolman, A., and Sarrat, C.: Mesoscale covariance of transport and CO_2 fluxes: Evidence from observations and simulations using the WRF - VPRM coupled atmosphere - biosphere model, J. Geophys. Res.-Atmos., 112, https://doi.org/10.1029/2007JD008552, 2007.

Berhanu, T. A., Szidat, S., Brunner, D., Satar, E., Schanda, R., Nyfeler, P., Battaglia, M., Steinbacher, M., Hammer, S., and Leuenberger, M.: Estimation of the fossil fuel component in atmospheric CO_2 based on radiocarbon measurements at the Beromünster tall tower, Switzerland, Atmos. Chem. Phys., 17, 10753-10766, https://doi.org/10.5194/acp-17-10753-2017, 2017.

Boon, A., Broquet, G., Clifford, D. J., Chevallier, F., Butterfield, D. M., Pison, I., Ramonet, M., Paris, J.-D., and Ciais, P.: Analysis of the potential of near-ground measurements of CO_2 and CH_4 in London, UK, for the monitoring of city-scale emissions using an atmospheric transport model, Atmos. Chem. Phys., 16, 6735-6756, https://doi.org/10.5194/acp-16-6735-2016, 2016.

Briber, B. M., Hutyra, L. R., Dunn, A. L., Raciti, S. M., and Munger, J. W.: Variations in atmospheric CO_2 mixing ratios across a Boston, MA urban to rural gradient, Land, 2, 304-327, https://doi.org/10.3390/land2030304, 2013.

Briber, B. M., Hutyra, L. R., Reinmann, A. B., Raciti, S. M., Dearborn, V. K., Holden, C. E., and Dunn, A. L.: Tree productivity enhanced with conversion from forest to urban land covers, PLoS One, 10, e0136237, https://doi.org/10.1371/journal.pone.0136237, 2015.

Cai, M., Ren, C., Shi, Y., Chen, G., Xie, J., and Ng, E.: Modeling spatiotemporal carbon emissions for two mega-urban regions in China using urban form and panel data analysis, Sci. Total Environ., 857, 159612, https://doi.org/10.1016/j.scitotenv.2022.159612, 2023.

Cai, Z., Che, K., Liu, Y., Yang, D., Liu, C., and Yue, X.: Decreased anthropogenic CO_2 emissions during the COVID-19 pandemic estimated from FTS and MAX-DOAS measurements at urban beijing, Remote Sens-basel., 13, 517, https://doi.org/10.3390/rs13030517, 2021.

Che, K., Liu, Y., Cai, Z., Yang, D., Wang, H., Ji, D., Yang, Y., and Wang, P.: Characterization of regional combustion efficiency using ΔXCO: ΔXCO_2 observed by a portable Fourier-Transform Spectrometer at an urban site in Beijing, Adv. Atmos. Sci., 39, 1299-1315, https://doi.org/10.1007/s00376-022-1247-7, 2022.

Chen, X., Zhang, F., and Zhao, K.: Diurnal variations of the land–sea breeze and its related precipitation over South China, J. Atmos. Sci., 73, 4793-4815, https://doi.org/10.1175/JAS-D-16-0106.1, 2016.

Chen, Y., Lu, Y., Qi, B., Ma, Q., Zang, K., Lin, Y., Liu, S., Pan, F., Li, S., and Guo, P.: Atmospheric CO_2 in the megacity

https://doi.org/10.5194/egusphere-2025-3215
Preprint. Discussion started: 4 September 2025

Hangzhou, China: Urban-suburban differences, sources and impact factors, Sci. Total Environ., 926, 171635, https://doi.org/10.1016/j.scitotenv.2024.171635, 2024.

Crippa, M., Guizzardi, D., Pisoni, E., Solazzo, E., Guion, A., Muntean, M., Florczyk, A., Schiavina, M., Melchiorri, M., and Hutfilter, A. F.: Global anthropogenic emissions in urban areas: patterns, trends, and challenges, Environ. Res. Lett., 16, https://doi.org/10.1088/1748-9326/ac00e2, 2021.

Crippa, M., Guizzardi, D., Pagani, F., Banja, M., Muntean, M., Schaaf, E., Monforti-Ferrario, F., Becker, W. E., Quadrelli, R., Risquez Martin, A., Taghavi-Moharamli, P., Köykkä, J., Grassi, G., Rossi, S., Melo, J., Oom, D., Branco, A., San-Miguel, J., Manca, G., Pisoni, E., Vignati, E., and Pekar, F.: GHG emissions of all world countries, Publications Office of the European Union, https://doi/10.2760/4002897, 2024.

Davies, Z. G., Edmondson, J. L., Heinemeyer, A., Leake, J. R., and Gaston, K. J.: Mapping an urban ecosystem service: quantifying above - ground carbon storage at a city - wide scale, J. Appl. Ecol., 48, 1125-1134, https://doi.org/10.1111/j.1365-2664.2011.02021.x, 2011.

Didan, K.: MOD13A3 MODIS/Terra Vegetation Indices Monthly L3 Global 1km SIN Grid V006, NASA Land Processes Distributed Active Archive Center [dataset], https://10.5067/MODIS/MOD13A3.006, 2015.

Dusenge, M. E., Duarte, A. G., and Way, D. A.: Plant carbon metabolism and climate change: elevated CO_2 and temperature impacts on photosynthesis, photorespiration and respiration, New Phytol., 221, 32-49, https://doi.org/10.1111/nph.15283, 2019.

Fasoli, B.: uataq/stilt: Geoscientific Model Development 2018 (v1.0), Zenodo [code], https://https://doi.org/10.5281/zenodo.1196561, 2018.

Fasoli, B., Lin, J. C., Bowling, D. R., Mitchell, L., and Mendoza, D.: Simulating atmospheric tracer concentrations for spatially distributed receptors: updates to the Stochastic Time-Inverted Lagrangian Transport model's R interface (STILT-R version 2), Geosci. Model Dev., 11, 2813-2824, https://doi.org/10.5194/gmd-11-2813-2018, 2018.

Feng, S., Jiang, F., Wang, H., Liu, Y., He, W., Wang, H., Shen, Y., Zhang, L., Jia, M., and Ju, W.: China's fossil fuel CO_2 emissions estimated using surface observations of coemitted NO_2, Environ. Sci. Technol., 58, 8299-8312, https://doi.org/10.1021/acs.est.3c07756, 2024.

Gao, S., Zhang, X., and Chen, M.: Spatiotemporal dynamics and driving forces of city-level CO_2 emissions in China from 2000 to 2019, J. Clean. Prod., 377, 134358, https://doi.org/10.1016/j.jclepro.2022.134358, 2022.

Gao, Y., Lee, X., Liu, S., Hu, N., Wei, X., Hu, C., Liu, C., Zhang, Z., and Yang, Y.: Spatiotemporal variability of the near-surface CO_2 concentration across an industrial-urban-rural transect, Nanjing, China, Sci. Total Environ., 631, 1192-1200, https://doi.org/10.1016/j.scitotenv.2018.03.126, 2018.

George, K., Ziska, L. H., Bunce, J. A., and Quebedeaux, B.: Elevated atmospheric CO_2 concentration and temperature across an urban–rural transect, Atmos. Environ., 41, 7654-7665, https://doi.org/10.1016/j.atmosenv.2007.08.018, 2007.

Gómez-Ortiz, C., Monteil, G., Basu, S., and Scholze, M.: A CO_2–$\Delta^{14}CO_2$ inversion setup for estimating European fossil CO_2 emissions, Atmos. Chem. Phys., 25, 397-424, https://doi.org/10.5194/acp-25-397-2025, 2025.

Gough, C. M. and Elliott, H. L.: Lawn soil carbon storage in abandoned residential properties: an examination of ecosystem structure and function following partial human-natural decoupling, J. Environ. Manage., 98, 155-162, https://doi.org/10.1016/j.jenvman.2011.12.028, 2012.

Griffin, R. J., Chen, J., Carmody, K., Vutukuru, S., and Dabdub, D.: Contribution of gas phase oxidation of volatile organic compounds to atmospheric carbon monoxide levels in two areas of the United States, J. Geophys. Res.-Atmos., 112, https://doi.org/10.1029/2006JD007602, 2007.

Han, P., Yao, B., Cai, Q., Chen, H., Sun, W., Liang, M., Zhang, X., Zhao, M., Martin, C., Liu, Z., Ye, H., Wang, P., Li, Y., and Zeng, N.: Support Carbon Neutral Goal with a High-Resolution Carbon Monitoring System in Beijing, B. Am. Meteorol. Soc., 105, E2461-E2481, https://doi.org/10.1175/bams-d-23-0025.1, 2024.

Han, S., Kondo, Y., Oshima, N., Takegawa, N., Miyazaki, Y., Hu, M., Lin, P., Deng, Z., Zhao, Y., and Sugimoto, N.: Temporal variations of elemental carbon in Beijing, J. Geophys. Res.-Atmos., 114, https://doi.org/10.1029/2009JD012027, 2009.

Hao, T., Chen, S., Liu, J., Tang, Y., and Han, S.: An observational study on the impact of sea-land breeze and low-level jet on

https://doi.org/10.5194/egusphere-2025-3215
Preprint. Discussion started: 4 September 2025

air pollutant transport in the Bohai Bay, Atmos. Pollut. Res., 15, 102143, https://doi.org/10.1016/j.apr.2024.102143, 2024.

Hao, T., Chen, S., Cai, Z., Shan, X., Meng, L., Han, S., and Dong, G.: Influence of sea breeze on atmospheric pollutant concentration over Tianjin, China Environmental Science, 37(9), 3247-3257, https://doi.org/10.3969/j.issn.1000-6923.2017.09.006, 2017.

He, H., Kramer, R. J., Soden, B. J., and Jeevanjee, N.: State dependence of CO_2 forcing and its implications for climate sensitivity, Science, 382, 7, https://doi.org/10.1126/science.abq6872, 2023.

Hersbach, H., Bell, B., Berrisford, P., Biavati, G., Horányi, A., Muñoz Sabater, J., Nicolas, J., Peubey, C., Radu, R., Rozum, I., Schepers, D., Simmons, A., Soci, C., Dee, D., Thépaut, J-N: ERA5 hourly data on single levels from 1940 to present, Copernicus Climate Change Service (C3S) Climate Data Store (CDS) [dataset], https://10.24381/cds.adbb2d47, 2023.

Hu, M., Wang, Y., Wang, S., Jiao, M., Huang, G., and Xia, B.: Spatial-temporal heterogeneity of air pollution and its relationship with meteorological factors in the Pearl River Delta, China, Atmos. Environ., 254, 118415, https://doi.org/10.1016/j.atmosenv.2021.118415, 2021.

Huang, Y., Li, S., Zhu, Y., Liu, Y., Hong, Y., Chen, X., Deng, W., Xi, X., Lu, X., and Fan, Q.: Increasing sea‐land breeze frequencies over coastal areas of China in the past five decades, Geophys. Res. Lett., 52, e2024GL112480, https://doi.org/10.1029/2024GL112480, 2025.

Ishidoya, S., Sugawara, H., Terao, Y., Kaneyasu, N., Aoki, N., Tsuboi, K., and Kondo, H.: O_2: CO_2 exchange ratio for net turbulent flux observed in an urban area of Tokyo, Japan, and its application to an evaluation of anthropogenic CO_2 emissions, Atmos. Chem. Phys., 20, 5293-5308, https://doi.org/10.5194/acp-20-5293-2020, 2020.

Jacobson, A. R., Schuldt, K. N., Andrews, A., Miller, J. B., Oda, T., Basu, S., Mund, J., Weir, B., Ott, L., Aalto, T., Abshire, J. B., Aikin, K., Allen, G., Andrade, M., Apadula, F., Arnold, S., Baier, B., Bakwin, P., Bartyzel, J., Bentz, G., Bergamaschi, P., Beyersdorf, A., Biermann, T., Biraud, S. C., Blanc, P.-E., Boenisch, H., Bowling, D., Brailsford, G., Brand, W. A., Brunner, D., Bui, T. P., Burban, B., Bäni, L., Calzolari, F., Chang, C. S., Chen, H., Chen, G., Chmura, L., Clark, S., Climadat, S., Colomb, A., Commane, R., Condori, L., Conen, F., Conil, S., Couret, C., Cristofanelli, P., Cuevas, E., Curcoll, R., Daube, B., Davis, K. J., De Mazière, M., De Wekker, S., Dean-Day, J. M., Della Coletta, J., Delmotte, M., Di Iorio, T., DiGangi, E., DiGangi, J. P., Dickerson, R., Elsasser, M., Emmenegger, L., Fang, S., Forster, G., France, J., Frumau, A., Fuente-Lastra, M., Galkowski, M., Gatti, L. V., Gehrlein, T., Gerbig, C., Gheusi, F., Gloor, E., Goto, D., Griffis, T., Hammer, S., Hanisco, T. F., Hanson, C., Haszpra, L., Hatakka, J., Heimann, M., Heliasz, M., Heltai, D., Henne, S., Hensen, A., Hermans, C., Hermansen, O., Hintsa, E., Hoheisel, A., Holst, J., Iraci, L. T., Ivakhov, V., Jaffe, D. A., Jordan, A., Joubert, W., Kang, H.-Y., Karion, A., Kawa, S. R., Kazan, V., Keeling, R. F., Keronen, P., Kim, J., Klausen, J., Kneuer, T., Ko, M.-Y., Kolari, P., Kominkova, K., Kort, E., Kozlova, E., Krummel, P. B., Kubistin, D., Kulawik, S. S., Kumps, N., Labuschagne, C., Lam, D. H., Lan, X., Langenfelds, R. L., Lanza, A., Laurent, O., Laurila, T., Lauvaux, T., Lavric, J., Law, B. E., Lee, C.-H., Lee, J., Lehner, I., Lehtinen, K., Leppert, R., Leskinen, A., Leuenberger, M., Leung, W. H., Levin, I., Levula, J., Lin, J., Lindauer, M., Lindroth, A., Loh, Z. M., Lopez, M., Lunder, C. R., Löfvenius, M. O., Machida, T., Mammarella, I., Manca, G., Manning, A., Manning, A., Marek, M. V., Marklund, P., Marrero, J. E., Martin, M. Y., Martin, D., Martins, G. A., Matsueda, H., McKain, K., Meijer, H., Meinhardt, F., Merchant, L., Metzger, J.-M., Mihalopoulos, N., Miles, N. L., Miller, C. E., Mitchell, L., Monteiro, V., Montzka, S., Moossen, H., Moreno, C., Morgan, E., Morgui, J.-A., Morimoto, S., Munger, J. W., Munro, D., Mutuku, M., Myhre, C. L., Mölder, M., Müller-Williams, J., Nakaoka, S.-I., Necki, J., Newman, S., Nichol, S., Nisbet, E., Niwa, Y., Njiru, D. M., Noe, S. M., Nojiri, Y., O'Doherty, S., Obersteiner, F., Paplawsky, B., Parworth, C. L., Peischl, J., Peltola, O., Peters, W., Philippon, C., Piacentino, S., Pichon, J. M., Pickers, P., Piper, S., Pitt, J., Plass-Dülmer, C., Platt, S. M., Prinzivalli, S., Ramonet, M., Ramos, R., Ren, X., Reyes-Sanchez, E., Richardson, S. J., Rigouleau, L.-J., Riris, H., Rivas, P. P., Rothe, M., Roulet, Y.-A., Ryerson, T., Ryoo, J.-M., Sargent, M., Sasakawa, M., Schaefer, H., Scheeren, B., Schmidt, M., Schuck, T., Schumacher, M., Seibel, J., Seifert, T., Sha, M. K., Shepson, P., Shin, D., Shook, M., Sloop, C. D., Smale, D., Smith, P. D., Spain, G., St. Clair, J. M., Steger, D., Steinbacher, M., Stephens, B., Sweeney, C., Sørensen, L. L., Taipale, R., Takatsuji, S., Tans, P., Thoning, K., Timas, H., Torn, M., Trisolino, P., Turnbull, J., Vermeulen, A., Viner, B., Vitkova, G., Walker, S., Watson, A., Weiss, R., Weyrauch, D., Wofsy, S. C., Worsey, J., Worthy, D., Xueref-Remy, I., Yates, E. L., Young, D., Yver-Kwok, C., Zaehle, S., Zahn, A., Zellweger, C., Zimnoch, M., de Souza, R. A., di Sarra, A. G., van

https://doi.org/10.5194/egusphere-2025-3215
Preprint. Discussion started: 4 September 2025

Dinther, D., and van den Bulk, P.: CarbonTracker CT-NRT.v2024-5, NOAA Earth System Research Laboratory [dataset], https://10.15138/atpd-k925, 2024.

Järvi, L., Nordbo, A., Junninen, H., Riikonen, A., Moilanen, J., Nikinmaa, E., and Vesala, T.: Seasonal and annual variation of carbon dioxide surface fluxes in Helsinki, Finland, in 2006–2010, Atmos. Chem. Phys., 12, 8475-8489, https://doi.org/10.5194/acp-12-8475-2012, 2012.

Kim, J., Berelson, W. M., Rollins, N. E., Asimow, N. G., Newman, C., Cohen, R. C., Miller, J. B., McDonald, B. C., Peischl, J., and Lehman, S. J.: Observing Anthropogenic and Biogenic CO_2 Emissions in Los Angeles Using a Dense Sensor Network, Environ Sci Technol, 59, 3508-3517, https://doi.org/10.1021/acs.est.4c11392, 2025.

Kumar, P.: Climate change and cities: challenges ahead, https://10.3389/frsc.2021.645613, 2021.

Kurppa, M., Nordbo, A., Haapanala, S., and Järvi, L.: Effect of seasonal variability and land use on particle number and CO_2 exchange in Helsinki, Finland, Urban. Clim., 13, 94-109, https://doi.org/10.1016/j.uclim.2015.07.006, 2015.

Lei, B.-Q., Li, L., and Chan, P. W.: Long-term trend in the sea-land breeze in Hong Kong, Urban. Clim., 55, 101981, https://doi.org/10.1016/j.uclim.2024.101981, 2024.

Leroyer, S., Bélair, S., Husain, S. Z., and Mailhot, J.: Subkilometer numerical weather prediction in an urban coastal area: A case study over the Vancouver metropolitan area, J. Appl. Meteorol. Clim., 53, 1433-1453, https://doi.org/10.1175/JAMC-D-13-0202.1, 2014.

Li, L., Mi, Y., Lei, Y., Wu, S., Li, L., Hua, E., and Yang, J.: The spatial differences of the synergy between CO_2 and air pollutant emissions in China's 296 cities, Sci. Total Environ., 846, 157323, https://doi.org/10.1016/j.scitotenv.2022.157323, 2022.

Lin, J. C., Bares, R., Fasoli, B., Garcia, M., Crosman, E., and Lyman, S.: Declining methane emissions and steady, high leakage rates observed over multiple years in a western US oil/gas production basin, Sci. Rep-uk., 11, 22291, https://doi.org/10.1038/s41598-021-01721-5, 2021.

Lin, J. C., Gerbig, C., Wofsy, S., Andrews, A., Daube, B., Davis, K., and Grainger, C.: A near‐field tool for simulating the upstream influence of atmospheric observations: The Stochastic Time‐Inverted Lagrangian Transport (STILT) model, J. Geophys. Res.-Atmos., 108(D16), https://doi.org/10.1029/2002JD003161, 2003.

Liu, C., Huang, J.-P., Diao, Y.-W., Wen, X.-F., Xiao, W., Zhang, M., Lee, X.-H., and Liu, S.-D.: Optimization and evaluation of vegetation photosynthesis and respiration model using the measurements collected from the forest site of subtropical coniferous-evergreen, Chinese Journal of Plant Ecology, 39, 388-397, https://doi.org/10.17521/cjpe.2015.0038, 2015.

Liu, H., Chan, J. C., and Cheng, A. Y.: Internal boundary layer structure under sea-breeze conditions in Hong Kong, Atmos. Environ., 35, 683-692, https://doi.org/10.1016/S1352-2310(00)00335-6, 2001.

Liu, W., Niu, Z., Feng, X., Zhou, W., Liang, D., Wang, G., and Liu, L.: Determining the key meteorological factors affecting atmospheric CO_2 and CH_4 using machine learning algorithms at a suburban site in China, Urban. Clim., 59, 102312, https://doi.org/10.1016/j.uclim.2025.102312, 2025.

Mai, B., Deng, X., Liu, X., Li, T., Guo, J., and Ma, Q.: The climatology of ambient CO_2 concentrations from long-term observation in the Pearl River Delta region of China: Roles of anthropogenic and biogenic processes, Atmos. Environ., 251, 118266, https://doi.org/10.1016/j.atmosenv.2021.118266, 2021.

Mai, B., Diao, Y., Yang, H., Deng, T., Zou, Y., Wang, Y., Lan, W., Liu, X., and Deng, X.: Assessing atmospheric CO_2 concentrations and contributions from biogenic and anthropogenic sources in the Pearl River Delta region, Urban. Clim., 54, 101864, https://doi.org/10.1016/j.uclim.2024.101864, 2024a.

Mai, J., Yu, L., Deng, T., Wu, D., Qing, P., and Yu, X.: Impact of sea-land breezes on the ozone pollution over the Pearl River Estuary, China Environmental Science, 45(03), 1198-1209, https://doi.org/10.19674/j.cnki.issn1000-6923.20241102.001, 2024b.

Melaas, E. K., Friedl, M. A., and Richardson, A. D.: Multiscale modeling of spring phenology across Deciduous Forests in the Eastern United States, Global Change Biol., 22, 792-805, https://doi.org/10.1111/gcb.13122, 2016a.

Melaas, E. K., Wang, J. A., Miller, D. L., and Friedl, M. A.: Interactions between urban vegetation and surface urban heat islands: a case study in the Boston metropolitan region, Environ. Res. Lett., 11, 054020, https://doi.org/10.1088/1748-9326/11/5/054020, 2016b.

https://doi.org/10.5194/egusphere-2025-3215
Preprint. Discussion started: 4 September 2025

Menzer, O. and McFadden, J. P.: Statistical partitioning of a three-year time series of direct urban net CO_2 flux measurements into biogenic and anthropogenic components, Atmos. Environ., 170, 319-333, https://doi.org/10.1016/j.atmosenv.2017.09.049, 2017.

Mitchell, L. E., Lin, J. C., Bowling, D. R., Pataki, D. E., Strong, C., Schauer, A. J., Bares, R., Bush, S. E., Stephens, B. B., and Mendoza, D.: Long-term urban carbon dioxide observations reveal spatial and temporal dynamics related to urban characteristics and growth, P. Natl. Acad. Sci. Usa., 115, 2912-2917, https://doi.org/10.1073/pnas.170239311, 2018.

Newman, S., Jeong, S., Fischer, M., Xu, X., Haman, C., Lefer, B., Alvarez, S., Rappenglueck, B., Kort, E., and Andrews, A.: Diurnal tracking of anthropogenic CO_2 emissions in the Los Angeles basin megacity during spring 2010, Atmos. Chem. Phys., 13, 4359-4372, https://doi.org/10.5194/acp-13-4359-2013, 2013.

Newman, S., Xu, X., Gurney, K. R., Hsu, Y. K., Li, K. F., Jiang, X., Keeling, R., Feng, S., O'Keefe, D., and Patarasuk, R.: Toward consistency between trends in bottom-up CO_2 emissions and top-down atmospheric measurements in the Los Angeles megacity, Atmos. Chem. Phys., 16, 3843-3863, https://doi.org/10.5194/acp-16-3843-2016, 2016.

Nie, X., Mao, H., Li, P., Li, T., Zhou, J., Wu, Y., Yang, M., Zhen, J., Wang, X., and Wang, Y.: Total gaseous mercury in a coastal city (Qingdao, China): Influence of sea-land breeze and regional transport, Atmos. Environ., 235, 117633, https://doi.org/10.1016/j.atmosenv.2020.117633, 2020.

Niu, Z., Zhou, W., Wu, S., Cheng, P., Lu, X., Xiong, X., Du, H., Fu, Y., and Wang, G.: Atmospheric fossil fuel CO_2 traced by $\Delta^{14}C$ in Beijing and Xiamen, China: temporal variations, inland/coastal differences and influencing factors, Environ. Sci. Technol., 50, 5474-5480, https://doi.org/10.1021/acs.est.5b02591, 2016.

Pan, C., Zhu, X., Wei, N., Zhu, X., She, Q., Jia, W., Liu, M., and Xiang, W.: Spatial variability of daytime CO_2 concentration with landscape structure across urbanization gradients, Shanghai, China, Clim. Res., 69, 107-116, https://doi.org/10.3354/cr01394, 2016.

Park, C., Jeong, S., Shin, Y.-s., Cha, Y.-s., and Lee, H.-c.: Reduction in urban atmospheric CO_2 enhancement in Seoul, South Korea, resulting from social distancing policies during the COVID-19 pandemic, Atmos. Pollut. Res., 12, 101176, https://doi.org/10.1016/j.apr.2021.101176, 2021.

Patz, J. A., Frumkin, H., Holloway, T., Vimont, D. J., and Haines, A.: Climate change: challenges and opportunities for global health, Jama, 312, 1565-1580, https://doi.org/10.1001/jama.2014.13186, 2014.

Pitt, J. R., Lopez-Coto, I., Hajny, K. D., Tomlin, J., Kaeser, R., Jayarathne, T., Stirm, B. H., Floerchinger, C. R., Loughner, C. P., and Gately, C. K.: New York City greenhouse gas emissions estimated with inverse modeling of aircraft measurements, Elem Sci Anth, 10, 00082, https://doi.org/10.1525/elementa.2021.00082, 2022.

Qiu, X. and Fan, S.: Progress of sea land breeze study and the characteristics of sea land breeze in three coastal areas in China, Meteorological Monthly, 39, 186-193, https://doi.org/10.7519/j.issn.1000-0526.2013.02.007, 2013a.

Qiu, X. and Fan, S.: Study on the application of auto-meteorological station data in local circulations analysis such as the sea-land breeze, Acta Scientiarum Naturalium Universitatis Sunyatseni, 52(2), 133-136, https://doi.org/10.13471/j.cnki.acta.snus.2013.02.025, 2013b.

Raciti, S. M., Hutyra, L. R., and Newell, J. D.: Mapping carbon storage in urban trees with multi-source remote sensing data: Relationships between biomass, land use, and demographics in Boston neighborhoods, Sci. Total Environ., 500, 72-83, https://doi.org/10.1016/j.scitotenv.2014.08.070, 2014.

Reddy, T. R., Mehta, S. K., Ananthavel, A., Ali, S., Annamalai, V., and Rao, D. N.: Seasonal characteristics of sea breeze and thermal internal boundary layer over Indian east coast region, Meteorol. Atmos. Phys., 133, 217-232, https://doi.org/10.1007/s00703-020-00746-1, 2021.

Rice, A. and Bostrom, G.: Measurements of carbon dioxide in an Oregon metropolitan region, Atmos. Environ., 45, 1138-1144, https://doi.org/10.1016/j.atmosenv.2010.11.026, 2011.

Schuldt, K. N., Mund, J., Aalto, T., Abshire, J. B., Aikin, K., Allen, G., Andrade, M., Andrews, A., Apadula, F., Arnold, S., Baier, B., Bakwin, P., Bartyzel, J., Bentz, G., Bergamaschi, P., Beyersdorf, A., Biermann, T., Biraud, S. C., Blanc, P.-E., Boenisch, H., Bowling, D., Brailsford, G., Brand, W. A., Brunner, D., Bui, T. P., Burban, B., Bäni, L., Calzolari, F., Chang, C. S., Chen, H., Chen, G., Chmura, L., Clark, S., Climadat, S., Colomb, A., Commane, R., Condori, L., Conen, F., Conil,

https://doi.org/10.5194/egusphere-2025-3215
Preprint. Discussion started: 4 September 2025

S., Couret, C., Cristofanelli, P., Cuevas, E., Curcoll, R., Daube, B., Davis, K. J., De Mazière, M., De Wekker, S., Dean-Day, J. M., Della Coletta, J., Delmotte, M., Di Iorio, T., DiGangi, E., DiGangi, J. P., Dickerson, R., Elsasser, M., Emmenegger, L., Fang, S., Forster, G., France, J., Frumau, A., Fuente-Lastra, M., Galkowski, M., Gatti, L. V., Gehrlein, T., Gerbig, C., Gheusi, F., Gloor, E., Goto, D., Griffis, T., Hammer, S., Hanisco, T. F., Hanson, C., Haszpra, L., Hatakka, J., Heimann, M., Heliasz, M., Heltai, D., Henne, S., Hensen, A., Hermans, C., Hermansen, O., Hintsa, E., Hoheisel, A., Holst, J., Iraci, L. T., Ivakhov, V., Jaffe, D. A., Jordan, A., Joubert, W., Kang, H.-Y., Karion, A., Kawa, S. R., Kazan, V., Keeling, R. F., Keronen, P., Kim, J., Klausen, J., Kneuer, T., Ko, M.-Y., Kolari, P., Kominkova, K., Kort, E., Kozlova, E., Krummel, P. B., Kubistin, D., Kulawik, S. S., Kumps, N., Labuschagne, C., Lam, D. H., Lan, X., Langenfelds, R. L., Lanza, A., Laurent, O., Laurila, T., Lauvaux, T., Lavric, J., Law, B. E., Lee, C.-H., Lee, J., Lehner, I., Lehtinen, K., Leppert, R., Leskinen, A., Leuenberger, M., Leung, W. H., Levin, I., Levula, J., Lin, J., Lindauer, M., Lindroth, A., Loh, Z. M., Lopez, M., Lunder, C. R., Löfvenius, M. O., Machida, T., Mammarella, I., Manca, G., Manning, A., Manning, A., Marek, M. V., Marklund, P., Marrero, J. E., Martin, M. Y., Martin, D., Martins, G. A., Matsueda, H., McKain, K., Meijer, H., Meinhardt, F., Merchant, L., Metzger, J.-M., Mihalopoulos, N., Miles, N. L., Miller, C. E., Miller, J. B., Mitchell, L., Monteiro, V., Montzka, S., Moossen, H., Moreno, C., Morgan, E., Morgui, J.-A., Morimoto, S., Munger, J. W., Munro, D., Mutuku, M., Myhre, C. L., Mölder, M., Müller-Williams, J., Nakaoka, S.-I., Necki, J., Newman, S., Nichol, S., Nisbet, E., Niwa, Y., Njiru, D. M., Noe, S. M., Nojiri, Y., O'Doherty, S., Obersteiner, F., Paplawsky, B., Parworth, C. L., Peischl, J., Peltola, O., Peters, W., Philippon, C., Piacentino, S., Pichon, J. M., Pickers, P., Piper, S., Pitt, J., Plass-Dülmer, C., Platt, S. M., Prinzivalli, S., Ramonet, M., Ramos, R., Ren, X., Reyes-Sanchez, E., Richardson, S. J., Rigouleau, L.-J., Riris, H., Rivas, P. P., Rothe, M., Roulet, Y.-A., Ryerson, T., Ryoo, J.-M., Sargent, M., Sasakawa, M., Schaefer, H., Scheeren, B., Schmidt, M., Schuck, T., Schumacher, M., Seibel, J., Seifert, T., Sha, M. K., Shepson, P., Shin, D., Shook, M., Sloop, C. D., Smale, D., Smith, P. D., Spain, G., St. Clair, J. M., Steger, D., Steinbacher, M., Stephens, B., Sweeney, C., Sørensen, L. L., Taipale, R., Takatsuji, S., Tans, P., Thoning, K., Timas, H., Torn, M., Trisolino, P., Turnbull, J., Vermeulen, A., Viner, B., Vitkova, G., Walker, S., Watson, A., Weiss, R., Weyrauch, D., Wofsy, S. C., Worsey, J., Worthy, D., Xueref-Remy, I., Yates, E. L., Young, D., Yver-Kwok, C., Zaehle, S., Zahn, A., Zellweger, C., Zimnoch, M., de Souza, R. A., di Sarra, A. G., van Dinther, D., and van den Bulk, P.: Multi-laboratory compilation of atmospheric carbon dioxide data for the period 1957-2023 (obspack_co2_1_test_GLOBALVIEWplus_v10.1_2024-11-13), NOAA Earth System Research Laboratory, Global Monitoring Laboratory [dataset], https://doi.org/10.25925/20241101, 2024.

Shan, Y., Wang, X., Wang, Z., Liang, L., Li, J., and Sun, J.: The pattern and mechanism of air pollution in developed coastal areas of China: From the perspective of urban agglomeration, PLoS One, 15, e0237863, https://doi.org/10.1371/journal.pone.0237863, 2020.

Shen, L., Zhao, C., and Yang, X.: Climate‐driven characteristics of sea‐land breezes over the globe, Geophys. Res. Lett., 48, e2020GL092308, https://doi.org/10.1029/2020GL092308, 2021.

Shusterman, A. A., Kim, J., Lieschke, K. J., Newman, C., Wooldridge, P. J., and Cohen, R. C.: Observing local CO_2 sources using low-cost, near-surface urban monitors, Atmos. Chem. Phys., 18, 13773-13785, https://doi.org/10.5194/acp-18-13773-2018, 2018.

Stauffer, R. M., Thompson, A. M., Martins, D. K., Clark, R. D., Goldberg, D. L., Loughner, C. P., Delgado, R., Dickerson, R. R., Stehr, J. W., and Tzortziou, M. A.: Bay breeze influence on surface ozone at Edgewood, MD during July 2011, J. Atmos. Chem., 72, 335-353, https://doi.org/10.1007/s10874-012-9241-6, 2015.

Sugawara, H., Ishidoya, S., Terao, Y., Takane, Y., Kikegawa, Y., and Nakajima, K.: Anthropogenic CO_2 emissions changes in an urban area of Tokyo, Japan, due to the COVID‐19 pandemic: A case study during the state of emergency in April–May 2020, Geophys. Res. Lett., 48, e2021GL092600, https://doi.org/10.1029/2021GL092600, 2021.

Sun, L., Tian, W., Zhang, W., Liu, C., and Fang, C.: Characteristics of sea-land breezes and their impact on $PM_{2.5}$ and O_3 in Shanghai and adjacent areas, Acta Scientiae Circumstantiae, 42(9), 339-350, https://doi.org/10.13671/j.hjkxxb.2022.0111, 2022.

Turnbull, J. C., Sweeney, C., Karion, A., Newberger, T., Lehman, S. J., Tans, P. P., Davis, K. J., Lauvaux, T., Miles, N. L., and Richardson, S. J.: Toward quantification and source sector identification of fossil fuel CO_2 emissions from an urban area:

https://doi.org/10.5194/egusphere-2025-3215
Preprint. Discussion started: 4 September 2025

Results from the INFLUX experiment, J. Geophys. Res.-Atmos., 120, 292-312, https://doi.org/10.1002/2014JD022555, 2015.

Velasco, E., Roth, M., Tan, S., Quak, M., Nabarro, S., and Norford, L.: The role of vegetation in the CO_2 flux from a tropical urban neighbourhood, Atmos. Chem. Phys., 13, 10185-10202, https://doi.org/10.5194/acp-13-10185-2013, 2013.

Verhulst, K. R., Karion, A., Kim, J., Salameh, P. K., Keeling, R. F., Newman, S., Miller, J., Sloop, C., Pongetti, T., and Rao, P.: Carbon dioxide and methane measurements from the Los Angeles Megacity Carbon Project–Part 1: calibration, urban enhancements, and uncertainty estimates, Atmos. Chem. Phys., 17, 8313-8341, https://doi.org/10.5194/acp-17-8313-2017, 2017.

Wang, B., Geddes, J. A., Adams, T. J., Lind, E. S., McDonald, B. C., He, J., Harkins, C., Li, D., and Pfister, G. G.: Implications of sea breezes on air quality monitoring in a coastal urban environment: Evidence from high resolution modeling of NO_2 and O_3, J. Geophys. Res.-Atmos., 128, e2022JD037860, https://doi.org/10.1029/2022JD037860, 2023.

Wang, P., Zhou, W., Niu, Z., Xiong, X., Wu, S., Cheng, P., Hou, Y., Lu, X., and Du, H.: Spatio-temporal variability of atmospheric CO_2 and its main causes: A case study in Xi'an city, China, Atmos. Res., 249, 105346, https://doi.org/10.1016/j.atmosres.2020.105346, 2021.

Wang, P., Zhou, W., Xiong, X., Wu, S., Niu, Z., Yu, Y., Liu, J., Feng, T., Cheng, P., and Du, H.: Source attribution of atmospheric CO_2 using ^{14}C and ^{13}C as tracers in two Chinese megacities during winter, J. Geophys. Res.-Atmos., 127, e2022JD036504, https://doi.org/10.1029/2022JD036504, 2022.

Wang, Y., Munger, J., Xu, S., McElroy, M. B., Hao, J., Nielsen, C., and Ma, H.: CO_2 and its correlation with CO at a rural site near Beijing: implications for combustion efficiency in China, Atmos. Chem. Phys., 10, 8881-8897, https://doi.org/10.5194/acp-10-8881-2010, 2010.

Wei, C., Wang, M., Fu, Q., Dai, C., Huang, R., and Bao, Q.: Temporal characteristics of greenhouse gases (CO_2 and CH_4) in the megacity Shanghai, China: Association with air pollutants and meteorological conditions, Atmos. Res., 235, 104759, https://doi.org/10.1016/j.atmosres.2019.104759, 2020.

Wei, D., Reinmann, A., Schiferl, L. D., and Commane, R.: High resolution modeling of vegetation reveals large summertime biogenic CO2 fluxes in New York City, Environ. Res. Lett., 17, 124031, https://doi.org/10.1088/1748-9326/aca68f, 2022.

WMO: WMO Greenhouse Gas Bulletin No. 20, Tech. rep., https://library.wmo.int/idurl/4/69057 (last access: 18 June 2025), 2024.

Wu, D., Lin, J. C., Duarte, H. F., Yadav, V., Parazoo, N. C., Oda, T., and Kort, E. A.: A model for urban biogenic CO_2 fluxes: Solar-Induced Fluorescence for Modeling Urban biogenic Fluxes (SMUrF v1), Geosci. Model Dev., 14, 3633-3661, https://doi.org/10.5194/gmd-14-3633-2021, 2021.

Wu, D., Liu, J., Wennberg, P. O., Palmer, P. I., Nelson, R. R., Kiel, M., and Eldering, A.: Towards sector-based attribution using intra-city variations in satellite-based emission ratios between CO_2 and CO, Atmos. Chem. Phys., 22, 14547-14570, https://doi.org/10.5194/acp-22-14547-2022, 2022a.

Wu, K., Davis, K. J., Miles, N. L., Richardson, S. J., Lauvaux, T., Sarmiento, D. P., Balashov, N. V., Keller, K., Turnbull, J., and Gurney, K. R.: Source decomposition of eddy-covariance CO_2 flux measurements for evaluating a high-resolution urban CO_2 emissions inventory, Environ. Res. Lett., 17, 074035, https://doi.org/10.1088/1748-9326/ac7c29, 2022b.

Xueref-Remy, I., Dieudonné, E., Vuillemin, C., Lopez, M., Lac, C., Schmidt, M., Delmotte, M., Chevallier, F., Ravetta, F., Perrussel, O., Ciais, P., Bréon, F.-M., Broquet, G., Ramonet, M., Spain, T. G., and Ampe, C.: Diurnal, synoptic and seasonal variability of atmospheric CO_2 in the Paris megacity area, Atmos. Chem. Phys., 18, 3335-3362, https://doi.org/10.5194/acp-18-3335-2018, 2018.

Yang, J. and Huang, X.: The 30 m annual land cover datasets and its dynamics in China from 1985 to 2024, Earth System Science Data [dataset], https://doi.org/10.5281/zenodo.15853565, 2025.

Yang, Y., Zhou, M., Wang, T., Yao, B., Han, P., Ji, D., Zhou, W., Sun, Y., Wang, G., and Wang, P.: Spatial and temporal variations of CO_2 mole fractions observed at Beijing, Xianghe, and Xinglong in North China, Atmos. Chem. Phys., 21, 11741-11757, https://doi.org/10.5194/acp-21-11741-2021, 2021.

Zhang, L., Lin, J., Shao, Y., Huang, S., Fan, S., and Wei, W.: Understanding the impact of sea and land breezes on ozone

https://doi.org/10.5194/egusphere-2025-3215
Preprint. Discussion started: 4 September 2025

pollution in the Pearl River Delta, Acta Scientiae Circumstantiae, 44(1), 74-85, https://doi.org/10.13671/j.hjkxxb.2023.0285, 2024.

Zhao, D., Xin, J., Wang, W., Jia, D., Wang, Z., Xiao, H., Liu, C., Zhou, J., Tong, L., and Ma, Y.: Effects of the sea-land breeze on coastal ozone pollution in the Yangtze River Delta, China, Sci. Total Environ., 807, 150306, https://doi.org/10.1016/j.scitotenv.2021.150306, 2022.

Zhao, T., Brown, D. G., Fang, H., Theobald, D. M., Liu, T., and Zhang, T.: Vegetation productivity consequences of human settlement growth in the eastern United States, Landscape Ecol., 27, 1149-1165, https://doi.org/10.1007/s10980-012-9766-8, 2012.

Zheng, Y., Jiang, F., Feng, S., Shen, Y., Liu, H., Guo, H., Lyu, X., Jia, M., and Lou, C.: Large-scale land-sea interactions extend ozone pollution duration in coastal cities along northern China, Env. Sci. Ecotechnol., 18, 100322, https://doi.org/10.1016/j.ese.2023.100322, 2024.

Zhu, X., Qin, Z., and Song, L.: How land‐sea interaction of tidal and sea breeze activity affect mangrove net ecosystem exchange?, J. Geophys. Res.-Atmos., 126, e2020JD034047, https://doi.org/10.1029/2020JD034047, 2021.